JGR Earth Surface

RESEARCH ARTICLE
10.1029/2022JF007000

Anatomy of an Alpine Bedload Transport Event: A Watershed-Scale Seismic-Network Perspective

Gilles Antoniazza[1,2], Michael Dietze[3,4], Davide Mancini[1], Jens M. Turowski[3], Dieter Rickenmann[2], Tobias Nicollier[2], Stefan Boss[2], and Stuart N. Lane[1]

[1]University of Lausanne, Institute of Earth Surface Dynamics (IDYST), Lausanne, Switzerland, [2]Swiss Federal Research Institute WSL, Mountain Hydrology and Mass Movements, Birmensdorf, Switzerland, [3]German Research Center for Geosciences (GFZ), Section 4.6 Geomorphology, Potsdam, Germany, [4]Faculty of Geosciences and Geography, Georg-August University Göttingen, Göttingen, Germany

Key Points:

- For the first time, a high-magnitude bedload transport event was tracked at the watershed scale by a network of 24 seismic sensors
- A comparatively low proportion of the material mobilized in the watershed during the event was exported at the outlet (2.5%)
- Multiple periods of competent flows are likely necessary to evacuate coarse material mobilized during individual bedload transport events

Supporting Information:

Supporting Information may be found in the online version of this article.

Correspondence to:

G. Antoniazza,
gilles.antoniazza@unil.ch

Citation:

Antoniazza, G., Dietze, M., Mancini, D., Turowski, J. M., Rickenmann, D., Nicollier, T., et al. (2023). Anatomy of an Alpine bedload transport event: A watershed-scale seismic-network perspective. *Journal of Geophysical Research: Earth Surface*, *128*, e2022JF007000. https://doi.org/10.1029/2022JF007000

Received 11 NOV 2022
Accepted 28 JUL 2023

Author Contributions:

Conceptualization: Gilles Antoniazza, Michael Dietze, Jens M. Turowski, Dieter Rickenmann, Tobias Nicollier, Stefan Boss, Stuart N. Lane
Data curation: Gilles Antoniazza, Michael Dietze, Davide Mancini, Jens M. Turowski
Formal analysis: Gilles Antoniazza, Michael Dietze, Davide Mancini, Jens M. Turowski, Dieter Rickenmann, Tobias Nicollier, Stuart N. Lane
Funding acquisition: Gilles Antoniazza

Abstract The way Alpine rivers mobilize, convey and store coarse material during high-magnitude events is poorly understood, notably because it is difficult to obtain measurements of bedload transport at the watershed scale. Seismic sensor data, evaluated with appropriate seismic physical models, can provide that missing link by yielding time-varying estimates of bedload transport albeit with non-negligible uncertainty. Low cost and ease of installation allow for networks of sensors to be deployed, providing continuous, watershed-scale insights into bedload transport dynamics. Here, we deploy a network of 24 seismic sensors to estimate coarse material fluxes in a 13.4 km^2 Alpine watershed during a high-magnitude transport event. First, we benchmark the seismic inversion routine with an independent time-series of bedload transport obtained with a calibrated acoustic system. Then, we apply the procedure to the other seismic sensors across the watershed. Propagation velocities derived from cross-correlation analysis between spatially consecutive bedload transport time-series were too high with respect to typical bedload transport velocity suggesting that a faster-moving water wave (re-)mobilizes local coarse material. Spatially distributed estimates of bedload transport reveal a relative inefficiency of Alpine watersheds in evacuating coarse material, even during a relatively infrequent high-magnitude bedload transport event. Significant inputs estimated for some tributaries were rapidly attenuated as the main river crossed less hydraulically efficient reaches. Only a small proportion of the total amount of material mobilized in the watershed was exported at the outlet. Multiple periods of competent flows are likely necessary to evacuate coarse material mobilized throughout the watershed during individual bedload transport events.

Plain Language Summary By driving erosion and deposition, bedload transport is a serious challenge for Alpine watershed management. Yet, the way Alpine rivers mobilize, convey, and store coarse material during high-magnitude events is poorly known, notably due to the difficulty of measuring bedload transport in different locations at the watershed scale. In this contribution, we use a network of 24 seismic sensors to capture the motion of coarse material in a 13.4 km^2 Alpine watershed during a high-magnitude bedload transport event. Collected bedload transport estimates revealed a relative inefficiency of Alpine watersheds in evacuating coarse material, even during a relatively high-magnitude bedload transport event. Large inputs estimated in some tributaries rapidly deposited as the flow crossed less transport-efficient reaches, and only a comparatively negligible proportion of the total amount of material mobilized in the watershed was exported at the outlet. Multiple periods of high streamflow are likely necessary to evacuate the coarse material mobilized throughout the watershed during individual bedload transport events. This data set increases knowledge of coarse material motion within Alpine watersheds during high-magnitude bedload transport events, and may help to improve predictions of bedload transport in the future through a better constraint on changing sediment availability in time and space.

1. Introduction

Bedload transport is an important component of watershed management within Alpine areas, through its conditioning of river morphology, the benefit it delivers to riverine ecosystems, and its important contribution to sediment budgets of lowland fluvial systems (A. Badoux et al., 2014, 2016; Wohl, 2006, 2013). Yet, the way Alpine watersheds produce, convey, and store coarse material is still poorly understood (Cavalli et al., 2013; Comiti et al., 2019; Dell'Agnese et al., 2015; Lane et al., 2017). This represents a major limit to the usefulness of

Investigation: Gilles Antoniazza, Michael Dietze, Jens M. Turowski, Stuart N. Lane
Methodology: Gilles Antoniazza, Michael Dietze, Davide Mancini, Jens M. Turowski, Stuart N. Lane
Project Administration: Stuart N. Lane
Resources: Michael Dietze, Stefan Boss, Stuart N. Lane
Software: Michael Dietze
Supervision: Stuart N. Lane
Validation: Gilles Antoniazza, Michael Dietze, Davide Mancini, Jens M. Turowski, Stuart N. Lane
Visualization: Gilles Antoniazza, Michael Dietze
Writing – original draft: Gilles Antoniazza, Michael Dietze, Davide Mancini, Jens M. Turowski, Dieter Rickenmann, Tobias Nicollier, Stefan Boss, Stuart N. Lane
Writing – review & editing: Gilles Antoniazza, Michael Dietze, Davide Mancini, Jens M. Turowski, Dieter Rickenmann, Stuart N. Lane

current bedload transport equations, since knowledge of change in sediment availability through time and space is needed for improving bedload transport predictions of steep (>5%) Alpine rivers (Gomez & Soar, 2022; Piton & Recking, 2017).

The morphology of Alpine rivers largely derives from their glacier legacy, with a typical long-profile comprising a succession of steep rockwalls and hillslopes, flatter and wider glacier troughs, and steeper glacier riegels (Antoniazza & Lane, 2021; S. L. Cook & Swift, 2012; Egholm et al., 2012; Hooke, 1991). Alpine rivers tend to develop different morphologies along reaches that present contrasting topographic and hydraulic properties. In the flatter reaches, usually covered by Quaternary material, the river is typically alluvial with plane-bed or braided morphologies (Comiti et al., 2019; Lane et al., 2017; Mao et al., 2017; Piton & Recking, 2017). In the steeper and sometimes more confined reaches, semi-alluvial reaches tend to develop cascades or step-pool morphologies (Recking et al., 2012; Turowski, 2012; Yager et al., 2012). Along semi-alluvial reaches, the streambed is made of a mixture of alluvial deposits and immobile or weakly mobile larger particles issuing from hillslope processes (e.g., landslides, debris flow), from deglaciation deposits, or from bedrock outcrops. The streambed is thus typically armored, resulting in limited sediment availability (Piton & Recking, 2017; Recking et al., 2012; Turowski et al., 2009; Yager et al., 2012). Alpine rivers are also often colluvial in their headwater reaches, which means that there may be intermittent and possibly important material supply from tributaries (Piton & Recking, 2017; Rainato et al., 2017).

The efficiency with which bedload is mobilized, transported and deposited may vary between these different morphological reaches (Comiti et al., 2019; Dell'Agnese et al., 2015; Lane et al., 2017). Alluvial reaches may alternatively act as sediment sources or sinks, but may not always be hydraulically efficient in conveying coarse material (Dell'Agnese et al., 2015; Lane et al., 2017; Mao et al., 2017). Semi-alluvial reaches are steeper, but also rougher, and evidence suggests that bedload may "travel" without major reworking of the underlying streambed along those reaches (Comiti et al., 2019; Coviello et al., 2022; Mueller & Pitlick, 2005; Piton & Recking, 2017; Recking et al., 2012). In colluvial systems, tributaries may supply material into the main channel, as long as their alluvial fans are not disconnecting the main river from the steep gullies draining the hillslopes (Lane et al., 2017; Mancini & Lane, 2020; Rainato et al., 2017). In this context, multiple studies have suggested a relative inefficiency of Alpine watersheds in conveying coarse material (Cavalli et al., 2013; Dell'Agnese et al., 2015; Lane et al., 2017; Rainato et al., 2017, 2018; Scorpio et al., 2022), but have also questioned the ability of high-magnitude flow events to increase hillslope coupling and to permit the efficient transfer of large amount of bedload through various morphological reaches of Alpine watersheds. To the authors' knowledge, this premise has been rarely tested with field data.

A primary reason for the lack of empirical support for limited coarse material transport efficiency is the difficulty of monitoring bedload transport throughout Alpine watersheds. Particle tracking experiments have provided insights into the motion of individual particles across different morphological reaches of Alpine watersheds (Dell'Agnese et al., 2015; Mao et al., 2017; Rainato et al., 2018; Schneider et al., 2014; Vázquez-Tarrío et al., 2019), but the extrapolation of individual particle motion to total bedload transfer is subject to substantial uncertainty. Repeated topographic surveys have also yielded information on coarse material dynamics (Antoniazza et al., 2019; Bakker et al., 2019; Comiti et al., 2019; Dai et al., 2021; Lane et al., 2017; Scorpio et al., 2022). But such techniques provide only poor temporal resolution, and cannot resolve processes during transport events. Recent progress in indirect acoustic sensing have allowed substantial advances in the continuous monitoring of bedload transport in natural settings (Antoniazza et al., 2022; Downing, 2010; Kreisler et al., 2017; Mizuyama et al., 2010; Rickenmann, 2018, 2020; Rickenmann et al., 2012, 2014b). Yet, the deployment of acoustic sensors in the river bed typically requires stable cross-sections (e.g., weirs) to be mounted efficiently, which may represent substantial installation costs and ecological impacts (Rickenmann, 2017), and limits the feasibility of monitoring bedload transport at multiple locations across Alpine watersheds.

Environmental seismology (K. L. Cook & Dietze, 2022) provides an alternative. Out-of-bank seismometers have been shown to record the energy emitted by bedload transport in a specific frequency band (Bakker et al., 2020; Burtin et al., 2011; Roth et al., 2016; Tsai et al., 2012). As this frequency is normally different to that associated with other fluvial processes, such as turbulence, time-varying estimates of bedload transport may be inferred (Bakker et al., 2020; Gimbert et al., 2019; Lagarde et al., 2021) through the inversion of appropriate physical models (Gimbert et al., 2014; Tsai et al., 2012). Compared to the setting of indirect acoustic sensors, passive seismic sensors are typically cheap, easy to deploy in a non-invasive way and require little maintenance such

that they can be distributed as networks to investigate bedload transport at multiple locations at the watershed scale (Chmiel et al., 2022; K. L. Cook et al., 2018; Coviello et al., 2019). Networks of seismic sensors have been deployed to investigate the dynamics of floods (Burtin et al., 2010; Chmiel et al., 2022; Piantini et al., 2022; Schmandt et al., 2017), debris flows (Chmiel et al., 2021; Coviello et al., 2019; Walter et al., 2017), and glacier lake outburst floods (K. L. Cook et al., 2018; Maurer et al., 2020). To date, no study has sought to collect time-varying spatially distributed seismic estimates of bedload transport in order to evaluate the efficiency of Alpine watersheds in conveying coarse material during a high-magnitude bedload transport event.

In this contribution, we estimate coarse material flux during a relatively high-magnitude bedload transport event (return period ∼1–2 years) throughout an Alpine watershed. To do so, we deployed a network of 24 seismic sensors across the 13.4 km^2 Vallon de Nant (VdN) watershed in the Swiss Alps, which alternates between alluvial, semi-alluvial and colluvial reaches. In a first step, we compare the time-varying estimates of bedload transport inverted from a seismic sensor with an independent time-series of bedload transport captured with a calibrated acoustic device located nearby, to evaluate the performance of the seismic inversion approach. Then, the same seismic approach is used to invert time-series of bedload transport from the other 23 seismic sensors distributed across the watershed, using local field-based measurements of the inversion model parameters. The resulting time-varying estimates are used to investigate coarse material fluxes at the watershed scale during the studied high-magnitude bedload transport event. Combined with a morphological change analysis, we discuss the efficiency of coarse material transfers in the watershed at the scale of the studied bedload transport event, and place it into a longer time-scale perspective.

2. Material and Methods

2.1. Study Site

The VdN is a 13.4 km^2 Alpine watershed located in South-Western Switzerland (Figure 1), at ∼1,200–∼3,050 m a.s.l. Through its position at the north-western margin of the European Alps, and due to the local high relief (notably on its eastern side), it forms a natural barrier to westerly and north-westerly air streams (Lane et al., 2016; Vittoz & Gmür, 2009). The VdN receives thus a substantial amount of annual precipitation (∼1,850 mm yr^{-1}), predominantly in summer (Antoniazza et al., 2022; Dutoit, 1983; Lane et al., 2016; Vittoz & Gmür, 2009). Given its high elevation, a significant proportion (∼45% in the year 2020) of annual precipitation occurs as snowfall (Antoniazza et al., 2022; Thornton et al., 2021, 2022), and snow cover may persist until late-spring to mid-summer in the less sun-exposed areas (e.g., valley bottom, gullies, hillslope base) of the watershed (Antoniazza et al., 2022; Dutoit, 1983; Lane et al., 2016; Thornton et al., 2021, 2022; Vittoz & Gmür, 2009). A small debris-covered glacier (Glacier des Martinets) occupies ∼3% of the watershed (in 2020), supplying only negligible amounts of ice melt. Thus, the hydrological regime of the watershed is dominated by snowmelt and rainfall (Antoniazza et al., 2022; Ceperley et al., 2020; Mächler et al., 2021; Michelon et al., 2021, 2022; Thornton et al., 2021, 2022).

Geologically, the watershed comprises rocks from the calcareous sedimentary series (limestones of Secondary age) belonging to the Helvetic domain (inverse flank of the "Nappes de Morcles—Doldenhorn"). There are also softer North-Helvetic Tertiary flyschs outcropping locally in the southern part of the watershed (Figure 1b, H. Badoux, 1971; Thornton et al., 2018). Whilst limestones are subject to karstification at different rates (i.e., depending on their composition), flyschs are expected to be much less permeable, which gives the VdN complex hydro-geological properties (Thornton et al., 2018, 2022). The geomorphology of the VdN largely derives from its glacial legacy (Antoniazza & Lane, 2021; S. J. Cook & Swift, 2012; Egholm et al., 2012; Hooke, 1991), with a typical "staircase" profile made of a succession of steep rockwalls and hillslopes, flatter glacier troughs, and steeper glacier riegels (Figure 1b). Bedrock only outcrops in the steeper reaches (i.e., rockwalls, riegels), while the flatter reaches (i.e., rockwall feet, glacier troughs) are covered by substantial depths (up to 80 m) of Quaternary till, which forms important aquifers (Thornton et al., 2022).

From the glacier snout (2,300 m a.s.l.), the Avançon de Nant (AdN) flows through a glacier trough (∼0.5 km, 17%; Reach 1 in Figure 1b) covered by Quaternary sediment (essentially moraines with depths between 10 and 50 m, Thornton et al., 2022), then through a steeper (∼0.3 km, 45%) riegel crossing a flysch outcrop (Reach 2), before reaching a flatter (∼1.7 km, 13%) Reach 3 in another glacier trough, with depths of Quaternary material between 10 and 80 m (Thornton et al., 2022). Along this reach, the AdN wanders between large Quaternary coalescent alluvial fans and develops a braided morphology, as an alluvial system. At the margin of the trough,

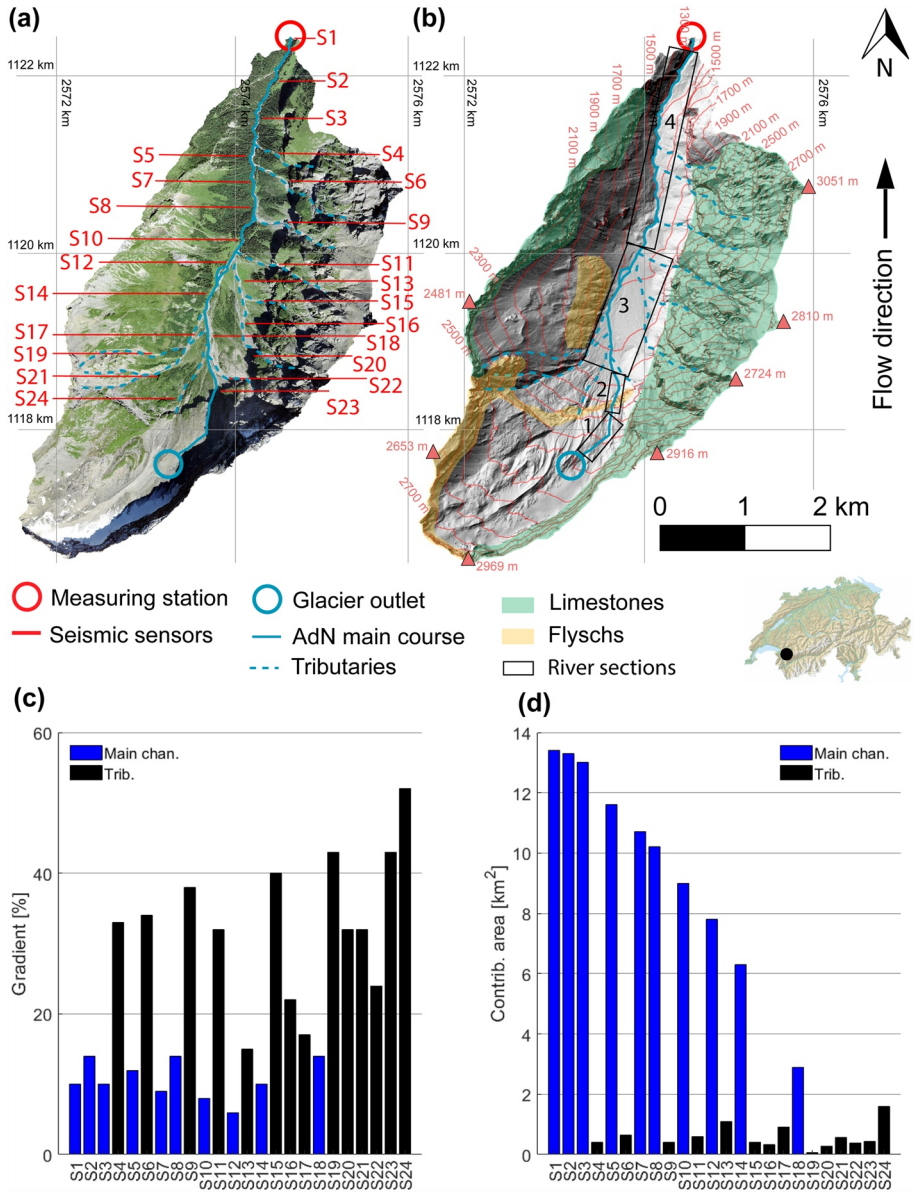

Figure 1. The Vallon de Nant Alpine watershed in (a) a 0.1-m resolution orthophoto (2020) and in (b) a hillshade (2020) based on the 0.5-m resolution LIDAR-based SwissAlti3d digital elevation model (Acknowledgments ©Swisstopo). Coordinates are provided in the CH1903+ Swiss system. The streamflow and Swiss Plate Geophone monitoring station at the outlet is labeled with a red circle. Seismic sensors deployed during the year 2020 are labeled S1–S24 from downstream to upstream in panel (a). The Glacier des Martinets outlet and the Avançon de Nant main course are labeled with a blue circle and blue line, respectively. The main temporarily flowing tributaries are labeled with a dashed blue line. In panel (b), the main bedrock outcrops are delineated in green (limestones of the "Nappe de Morcles-Doldenhorn") and in yellow (flyschs of the Northern Helvetic), the rest of the surface in gray being covered by Quaternary sediment. Numbered black boxes in panel (b) are used to differentiate between different river reaches in the text description. In panels (c, d) respectively, channel gradient (%) and contributing area (km^2) at each of the 24 seismic sensor location of the main channel (in blue) and tributaries (in black).

the AdN enters a more topographically constrained Reach 4, and alternates between semi-alluvial step-pool and alluvial wandering reaches (~2.9 km, 9%). The AdN is also fed by ~10 steep (35%–50%) tributaries (dashed blue lines in Figure 1a) that are mainly active during the snowmelt season, or briefly during storm events (i.e., colluvial system), and which form large coalescent fans at the hillslope base (Antoniazza et al., 2022; Lane et al., 2016; Figure 1a). They essentially feed the AdN main course in Reaches 3 and 4, and alternatively cross limestone outcrops, flysch outcrops and/or Quaternary deposits (Figure 1b). Their setting may make them possibly prone

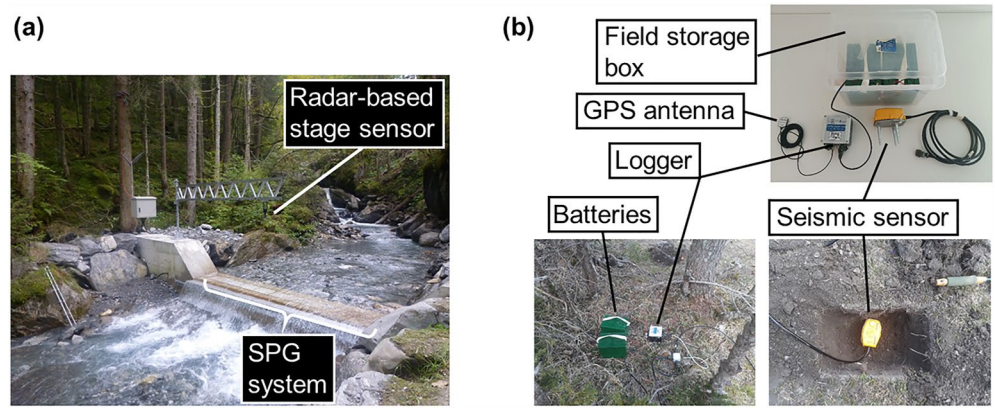

Figure 2. In (a), monitoring station at the Vallon de Nant outlet. Streamflow is continuously measured through a calibrated radar-based stage sensor, and 10 calibrated units of the Swiss Plate Geophone system provide a continuous monitoring of bedload transport. In panel (b), the seismic equipment (logger, sensor, GPS antenna, batteries, and storage box) used in this study, with an example of field setting.

to both bedload transport events as well as debris flow or debris flood events (Lane et al., 2016; Rickenmann & Koschni, 2010).

To capture the motion of coarse material throughout the VdN, a network of 24 seismic sensors was deployed across the VdN during the year 2020. Sensors were installed to detect signal from the AdN main channel, and the major tributary inputs (Figure 1a). Thus, the sensors covered ~9,800 m of channel length, with an average of one sensor per ~400 m of channel. Channel gradient and contributing area at each seismic sensor location are reported in Figures 1c and 1d, respectively. Channel gradient is lower within the main channel (e.g., S1, S3, S5, S7, S10), and greater in the tributaries feeding it (e.g., S4, S6, S9, S11). The gradient also tends to increase towards the watershed head, where multiple steeper tributaries combine to form the AdN main channel (Figure 1c). Contrastingly, contributing area (Figure 1d) decreases upstream, and seismic sensors located within the AdN main channel drain a much larger area than the tributaries feeding them. There is a negative power law relationship between gradient G and contributing area CA, such as $G = 23 * CA^{-0.33}$ ($R^2 = 0.71$).

Between 2014 and 2015, a hydrological and bedload transport monitoring station (Figure 2a) was built at the outlet of the watershed (1,200 m a.s.l.; red circle in Figures 1a and 1b) through a collaboration between the University of Lausanne, the Swiss Federal Institute for Forest, Snow and Landscape Research WSL, and the ETH Zürich (Physics of Environmental Systems). Since 2016, it allows for continuous monitoring of both streamflow and bedload transport (1-min resolution), through a calibrated radar-based stage sensor, and 10 calibrated units of a Swiss Plate Geophone (SPG) system (Rickenmann et al., 2012, 2014b), respectively. Antoniazza et al. (2020, 2022) and (Nicollier, Antoniazza, Ammann, et al., 2022; Nicollier, Antoniazza, Rickenmann, et al., 2022) describe the system and its calibration in detail. In this contribution, we used data from the monitoring station (a) to set the investigated bedload transport event into comparative context with other events that took place over the period 2016–2020 and (b) as a benchmark method to evaluate the seismic inversion approach for bedload transport sensing. Note that the two bedload transport monitoring systems may have different capabilities in terms of minimal grain-size detection, which may translate into differences in bedload transport estimates. The SPG system has a detection threshold for particles greater than ~10–20 mm (Nicollier et al., 2021; Nicollier, Antoniazza, Ammann, et al., 2022; Nicollier, Antoniazza, Rickenmann, et al., 2022; Wyss et al., 2016a, 2016b, 2016c), while seismic inversion may detect smaller particles if hydraulic and transport conditions allow it.

2.2. Seismic Inversion Approach

2.2.1. Seismic Monitoring

This study focuses on a relatively high magnitude bedload transport event (return period ~1–2 years) that took place on 3 August 2020, the largest captured in the seismic monitoring. In addition to the outlet SPG monitoring station, the event was simultaneously detected by a network of 24 seismic stations comprising 4.5 Hz PE6/B geophones and Cube3ext loggers (DiGOS, Germany), installed across the VdN watershed (Figures 1a and 2b).

One of the seismic sensors was installed next to the SPG monitoring station to be able to evaluate the performance of the seismic inversion approach in this environment. Following Bakker et al. (2020), each sensor was placed at 5–30 m from the channel, buried at ∼0.3 m underground to be isolated from surface seismic noise (e.g., rainfall, wind), oriented to the north and leveled horizontally (Figure 2b). The loggers were set to record the seismic signal with a frequency of 200 Hz, and a gain of 32. They were powered by two 9 V–200 Ah air alkaline batteries mounted in parallel. An internal active GPS antenna (BY-GPS-07) also recorded time continuously (Figure 2b), allowing synchronization of the data of the different seismic loggers, as well as the ones of the monitoring station (Figure 2a).

2.2.2. Seismic Model Application

In order to inverse time-varying bedload transport estimates from the seismic signal recorded by each sensor, a mixed turbulence (Gimbert et al., 2014) and bedload transport (Tsai et al., 2012) treatment, "Fluvial Model Inversion" (FMI), was applied (after Dietze et al. (2019)). This used an open source R package "eseis" (v. 0.4.0) (Dietze, 2018). The approach assumes that the seismic spectrum recorded near a river during a bedload transport event is dominated by a combination of force fluctuations in the fluid due to turbulence and coarse particles impacting the bed (Bakker et al., 2020; Dietze et al., 2019; Gimbert et al., 2019; Schmandt et al., 2017), which result in seismic power in different, yet overlapping frequency bands. The turbulence model of Gimbert et al. (2014) predicts the power spectral density (PSD) of vertical Raleigh waves induced by the flow interacting with roughness elements present along both the bed and the banks. The bedload transport model of Tsai et al. (2012) predicts the PSD of vertical Raleigh waves generated by the impacts of saltating particles on the riverbed, assuming that the coarsest particles in transport ($>D_{90}$) are responsible for the largest seismic signal recorded (Bakker et al., 2020; Dietze et al., 2019; Gimbert et al., 2019; Lagarde et al., 2021; Tsai et al., 2012). The FMI uses a least-squared procedure to fit the measured empirical seismic spectrum to synthetic ones produced by the paired models for random combinations of water depth h and unit bedload transport rate q_b estimated within their own plausible range, to invert the most likely values of h and q_b at each targeted time-step (Dietze et al., 2019).

Bedload transport and water depths were inverted from the paired FMI, requiring constraints on nine parameters, which can be separated into three classes following Lagarde et al. (2021); (a) the river morphology parameters, which include the channel gradient θ (radians), the channel width W (m), and the distance between the channel centerline and the seismic sensor r_0 (m); (b) the grain-size distribution (GSD) parameters, which include the median grain-size D_{50} (m) and the standard deviation σ_g (–) of a parametric log-raised cosine function fitted to discrete measured particle classes (Tsai et al., 2012); and (c) the seismic ground properties, which are described by Green's function as (Bakker et al., 2020; Tsai et al., 2012):

$$v_p = v_{p0}(f/f_0)^{-\xi} \tag{1a}$$

$$v_g = v_p/(1+\xi) \tag{1b}$$

$$K = K_0(f/f_0)^{\eta} \tag{1c}$$

where, v_p is the phase velocity of the Raleigh wave (m s^{-1}), v_{p0} is the phase velocity of the Raleigh wave at a frequency $f_0 = 1$ Hz, f is the frequency (Hz), ξ (–) a dimensionless exponent used to scale a frequency-dependent decay in seismic signal, v_g the wave group velocity (m s^{-1}), K (–) a dimensionless quality factor, K_0 (–) a dimensionless quality factor at a frequency $f_0 = 1$ Hz, and η (–) a dimensionless exponent that expresses the change in the quality factor K with frequency. To these nine site-specific parameters, two constants complete the paired FMI: the water density $\rho_w = 1{,}000$ kg m^{-3} and the sediment density $\rho_s = 2{,}650$ kg m^{-3}.

2.2.3. Model Parameterization

The river morphology parameters were derived from RTK-dGPS survey using a Trimble R10 device, combined with measurements performed on a 0.1-m resolution orthophoto (2020) and a 0.5-m resolution Alti3d Digital Elevation Model (2020) from the aerial campaigns of the Swiss Federal Office of Topography (Swisstopo). For each of the 24 seismic stations, the position of the seismic sensor was measured to derive the sensor-to-river distance r_0; the positions of both channel edges were identified to derive the channel width W; and the average channel gradient θ was computed over a reach of ∼100 m encompassing the seismic sensor location. The coordinates of the 24 seismic sensor locations, together with the river morphology parameters measured at each site, are available in Text S1 in Supporting Information S1.

The GSD parameters were derived from a line-by-number count (Wolman, 1954) of 100 mobile particles on the riverbed (Bakker et al., 2020; Lagarde et al., 2021) performed at each of the 24 seismic sensor locations. The particles were then separated into 10 size classes (Bakker et al., 2020; Text S2 in Supporting Information S1), and the parameters D_{50} and σ_g were derived following Tsai et al. (2012) from a best-fit log-raised cosine function out of 10^4 runs. The GSD parameters measured at each of the 24 seismic sensor locations are available in Text S2 in Supporting Information S1.

The seismic ground property parameters were derived from an active seismic survey undertaken individually for each seismometer following Bakker et al. (2020). In a first experiment, a second seismic sensor was installed on the opposite bank from a given seismic station targeted for the ground seismic parameterization. Both loggers were set to record at 800 Hz in order to capture the active seismic signal at the highest possible rate. A metallic plate with dimensions $0.3 \times 0.3 \times 0.01$ m (thickness) and a mass of ∼15 kg was set in line with the two seismic stations, and its position was recorded using a RTK-dGPS Trimble R10 device. The line made by the two seismic stations and the impact plate was orthogonal to the streamflow, and the impact plate was set at one end of the line. During periods of low streamflow to minimize signal contamination by turbulence, the plate was repeatedly struck 20 times using a sledgehammer, in order to derive for each impact the decay in surface wave velocity v_g with frequency, according to the arrival time of the active seismic signal at the two sensors. To do so, we first deconvolved the raw seismic signal according to the sensor characteristics. We also removed the mean and the seismic signal was detrended to avoid artifacts in the calculation of the PSD function (Lagarde et al., 2021). Following Bakker et al. (2020), the seismic signal was band-pass filtered for 50% overlapping intervals of 6 Hz, and a Hilbert envelope was calculated to identify the signal peak amplitude of each hammer blow. Knowing both distance and arrival time delay (i.e., in peak amplitude) between the active seismic source and the sensors, the surface wave velocity v_g was derived, and its decay with frequency allowed to constrain parameters v_{p0} and ξ in Equations 1a and 1b.

In a second experiment, the position of the impact plate was changed multiple times (∼4–10) to vary the distance (∼5–100 m) between the seismic sensor and the active seismic source. At each impact location, the position of the plate was measured using an RTK-dGPS Trimble R10, and 20 consecutive impacts were performed using the sledgehammer. This experiment was used to quantify the attenuation in seismic power with distance to the seismic source K (or quality factor, Equation 1c), and assess its frequency dependency (η in Equation 1c). To do so, signal spectrograms were computed from the detrended seismic signal using the Welch's method (Welch, 1967), averaging seismic power at 1 s intervals using 80% overlapping sub-windows of 0.5 s.

The active seismic experiments were repeated at each seismic sensor location to derive site-specific ground seismic properties, with the exceptions of sensor groups S10–S12, S16–S20, and S22–S24, where a single active seismic experiment encompassing each group of sensors was performed, thanks to their geographical proximity. Parameters v_{p0} and ξ from Equations 1a and 1b, and parameters K_0 and η from Equation 1c, estimated at each of the 24 seismic sensor locations based on active seismic experiments, are reported in Text S3 in Supporting Information S1.

2.2.4. Model Application

Using the parameters determined in 2.2.3, combined with the full range of possible water levels h (0.1–1 m) and unit bedload transport rates q_b (10^1–10^5 kg min^{-1}) estimated from the monitoring station data and from data sets of bedload transport events in comparable settings (Comiti et al., 2019; Coviello et al., 2022; Picco et al., 2012; Recking, 2013; Rickenmann, 2001, 2023), 2×10^4 synthetic spectra are produced in the FMI, and compared to the empirical spectrum in a least-squared procedure (Dietze, 2018; Dietze et al., 2019). Doing so, the values of h and q_b minimizing the error between the synthetic and the empirical spectra are determined at 1-min resolution. Since we are interested in bedload transport, the inversion is performed focusing on a range of frequencies (25–60 Hz) in which bedload noise is normally found (Bakker et al., 2020; Schmandt et al., 2017; Tsai et al., 2012), optimizing the inversion of q_b at the expense of h. This procedure is applied to every sensor, providing with 24 time-varying estimates of bedload transport, at 1-min resolution, over the duration of the 3 August 2020 event and distributed across the VdN watershed.

The main focus of the study is to perform seismic inversion of bedload transport specifically. As the high frequencies (i.e., 25–60 Hz) related to bedload transport in the seismic signal tend to attenuate more rapidly than the lower frequencies (i.e.,<20 Hz) related to turbulence (Gimbert et al., 2014; Tsai et al., 2012), the seismometers

were located close to the stream (~5–30 m). In this configuration, former research has shown that the bedload transport signal tends to outweigh the signature of river turbulence in the frequency range characteristic of bedload transport (Bakker et al., 2020; K. L. Cook & Dietze, 2022). In addition, the surveyed river exhibits a series of protruding roughness elements that likely form standing waves. This has been shown (Nativ et al., 2022; Schmandt et al., 2013, 2017) to generate seismic signals not accounted for by the turbulence model (Gimbert et al., 2014). For those reasons, the water level inversion h is not accurate in our setting, and we do not further consider it in the frame of this study. To illustrate it, the mean empirical spectrum recorded by each of the 24 seismometers is provided in Text S4 in Supporting Information S1, following Dietze et al. (2022b). It indeed shows that seismic energy in the frequency band specific of bedload transport (25–60 Hz) outweighs the seismic power in the frequency band specific of turbulence (<20 Hz) at each of the 24 seismic sensor locations.

A number of recent studies have shown the relatively good performance of the FMI model to retrieve bedload transport estimates (Dietze et al., 2019, 2022a; Lagarde et al., 2021). Yet, multiple sources of uncertainty were shown to possibly affect the performance of the bedload transport inversion. It notably includes (a) the possible discrepancy between the assumptions of the theoretical model (e.g., particle vertical impact; Tsai et al., 2012) and the process sensed in the field; (b) the right partitioning by the model of the seismic energy released by either turbulence or bedload transport; (c) the contamination of the seismic signal by noise sources that are external to the river (e.g., rainfall); (d) spatial averaging of the river seismic signal, because seismometers may not only detect ground vibrations at the cross-section where there are deployed, but also over a certain distance upstream and downstream; (e) a representative estimate of the model parameters that drives the inversion, and how those may be changing through time; and (f) bedload transport inversion in steep and rough tributaries. The general objective of this paper is not to improve the performance of the FMI model further, but to apply the approach (Bakker et al., 2020; Dietze et al., 2019, 2022a; Gimbert et al., 2014; Lagarde et al., 2021; Tsai et al., 2012) to obtain time-varying estimates of bedload transport at different locations of an Alpine watershed, which was to the authors' knowledge never achieved to date. Nevertheless, we evaluate the performance of the seismic inversion approach by comparing retrieved bedload transport estimates with the independent SPG measurement, and we further constrain and discuss how different sources of uncertainties may affect the bedload transport estimates we invert.

2.3. Data Analysis

2.3.1. Seismic Inversion Strategy

The seismic inversion approach was first applied to the data recorded by the seismic sensor that was located near to the SPG monitoring station (~20 m). This allowed the seismic-inverted time-varying estimates to be compared to a second and independent measurement of bedload transport over the duration of the event of interest, allowing assessment of the inversion approach. After evaluation, the same seismic inversion approach was applied to the other 23 sensors distributed in the VdN watershed but using the site-specific measured parameters following the procedure described in Sections 2.2.3 and 2.2.4.

2.3.2. Summary Statistics for the 24 Time-Varying Estimates of Bedload Transport

Once the inversion procedure was applied to the 24 seismic sensors, spatially distributed time-varying estimates of bedload transport were obtained for the event of interest. Three statistics were used to characterize the bedload transport event inverted at each seismic sensor location: (a) the estimated mass of coarse material transported over the event duration; (b) the timing of the start and end of the bedload transport event, and the timing of the major (multiple hours in duration) bedload transport waves; and (c) the temporal lag and propagation velocity of bedload transport between pairs of spatially consecutive seismic sensors.

Objective criteria applicable to every time-varying bedload transport estimates were used to automatically determine these statistics. An example of how this was done is provided in Figure 3 for sensor S1 located near to the monitoring station and where two major bedload transport waves were identified. Note that the developed procedure can be indifferently applied to retrieve these statistics for one or multiple bedload transport waves.

At step (i), we calculated a cumulative sum of bedload transport estimates over the duration of the event for each sensor (blue line in Figure 3a). At step (ii), we fitted a smoothing spline to each cumulative distribution (dashed red line in Figure 3a). At step (iii), we calculated the second derivative of the spline (blue line in Figure 3b) to

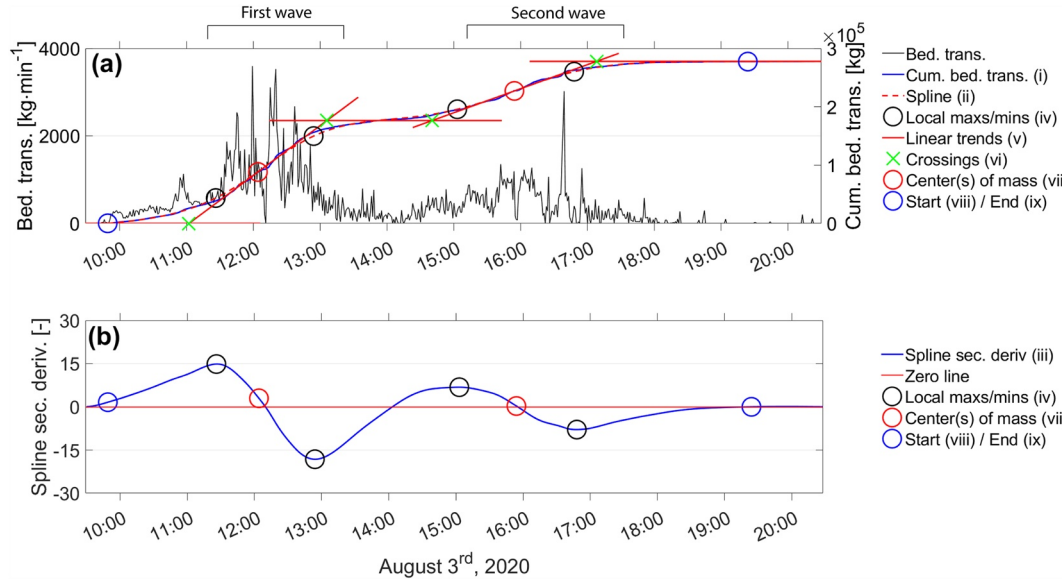

Figure 3. Example of the procedure applied to each of the 24 seismic-inverted time-varying bedload transport estimates to determine: (1) the estimated mass of coarse material transported over the event duration, (2) the timing of the event start and end, and the timing of the major (multiple hours in duration) bedload transport waves, and (3) the temporal lag and propagation velocity of bedload transport between spatially consecutive seismic sensors. The example is provided for seismic sensor S1 located near to the monitoring station, where two major bedload waves were identified. In panel (a), the seismic-inverted time-varying estimate of bedload transport and associated cumulative distribution. In panel (b), the second derivative of the smoothing spline fit.

obtain (iv) inflexion points (i.e., local maxima and minima in the second derivative; black circles in Figures 3a and 3b). At step (v), we calculated the equation of the lines meeting each pair of consecutive inflexion points (red lines in Figure 3a). The slope coefficient of the lines before, in-between and after any bedload wave was set to zero, and the crossing points between trend lines (green crosses in Figure 3a) was retained as the start and end points of each major bedload wave (vi). At step (vii), we computed the center of mass of each major bedload wave (red circles in Figures 3a and 3b), by taking the mid-point between trend line crossings marking a linear increase in the spline fit. At step (viii), the start point of the bedload transport event was set at the crossing between the spline fit and bedload transport rate zero line. At step (ix), the end of the bedload transport event was determined as the point from which the spline fit reaches an upper plateau (i.e., a second derivative greater than −0.01; blue circles in Figures 3a and 3b).

Integration of the bedload transport estimates between the start (vii) and end points (viii) gave us (1) the estimated mass of coarse material transported over the duration of the event at each seismic sensor location. It allows estimation of changes in the coarse material transport across the watershed during the studied bedload transport event. The timing of the bedload transport start (vii) and end (viii) points, as well as the timing of the major bedload transport waves (vi), allowed us to calculate (2) to compare the timing of the bedload transport event at the different seismic sensor locations. To characterize the temporal lag between time-series of bedload transport inverted at two spatially consecutive seismic sensors, and the associated propagation velocity, a cross-correlation analysis was performed. Using the distance between two spatially consecutive sensors measured on a 0.1-m resolution orthophoto of 2020, propagation velocities between pairs of spatially consecutive sensors were computed to obtain (3).

2.3.3. Morphological Change Analysis

In order to place the 3 August 2020 bedload transport event into a longer-term perspective of sediment fluxes throughout Alpine watersheds, we perform a morphological change analysis. It is derived from two 0.5-m resolution LIDAR-based (Swisstopo aerial campaigns) SwissAlti3d digital elevation models (DEM) of 2016 (25 August) and 2020 (6 August), which were derived from two point clouds with an initial mean density of 15–20 pts m^{-2} (Swisstopo, 2022). In a first step, we verified the co-registration of the two Swisstopo DEMs by computing the distribution of errors between stable areas of the two DEMs (Cucchiaro et al., 2020; Minute et al., 2019;

Pitscheider et al., 2022). Selected stable areas (i.e., grassy lands, bedrock) covered all together ~0.12 km^2, were evenly distributed across the watershed, and presented various degrees of slope (i.e., valley bottom, hillslopes). A systematic error of $\mu = 0.16$ m ($\sigma = \pm 0.11$ m) was identified between the two Swisstopo DEMs. We applied a best-fit function between the stable areas of the two DEMs to model the co-registration error. Error in Z for each pair of XY coordinates was minimized by applying the following correction:

$$\text{Error}_Z = p_{00} + p_{10} * X + p_{01} * Y \quad (2)$$

where Error_Z (m) is the modeled vertical co-registration error, $p_{00} = 290.2$, $p_{10} = -1.364 \times 10^{-4}$ and $p_{01} = 0.5455 \times 10^{-4}$ are coefficients, X (m) are easting coordinates and Y (m) northing coordinates. We applied the correction to every pair of XY cells of the DEM of 2021, and removed the modeled error Error_Z from the elevation Z of the DEM of 2021. Distribution of error in the same stable areas between the DEM of 2019, and the corrected DEM of 2021, showed a reduced error with $\mu = -0.07$ m and $\sigma = \pm 0.09$ m. Once DEM co-registration was optimized, the altitude of the DEM of 2019 were subtracted cell-by-cell from the altitude of the DEM of 2021 in order to obtain erosion and deposition depths across the watershed area over the survey interval. Volumetric changes were then obtained by multiplying cumulated vertical changes by the DEM cell resolution (0.5×0.5 m). A threshold of detection was set as LoD = ± 0.2 m, corresponding to approximately twice the standard deviation of the residual error after co-registration.

To increase the efficiency of the morphological change analysis, and to avoid potentially large errors in the steep rockwall zones (Minute et al., 2019; Pitscheider et al., 2022) present throughout the watershed, we followed former research that has limited morphological change analysis to the Sediment Contributing Area (SCA) (Altmann et al., 2021; Cavalli et al., 2017; Minute et al., 2019; Pitscheider et al., 2022); that is all sedimentary sources connected by active non-vegetated channels to the main drainage network. The delineation of the SCA was done using the Swisstopo 0.1-m resolution orthophoto of 2020. Patterns of erosion and deposition encompass the effects of the 3August 2020 bedload transport event, but also multiple other bedload transporting events that have taken place in this time interval (Antoniazza et al., 2022). Note that while seismic sensing detects bedload transport only, morphological change analysis may also include finer material transported in suspension.

3. Results

3.1. The 3 August 2020 Bedload Transport Event

Météosuisse datasets RhiresD and TabsD (MétéoSuisse, 2017, 2019) of daily precipitation and daily mean temperature show that 57.4 mm of precipitation (with a mean daily temperature of 5.75°C) fell over the VdN on 3 August 2020, likely as rainfall given the >1°C daily mean temperature. The hydrological analysis performed by Antoniazza et al. (2022) further indicates that there was also a strong sub-daily discharge cycle on 3 August 2020 (outside of rainfall events) meaning that a signal related to snowmelt was present in the watershed, and that baseflow was still relatively high (~0.5 m^3 s^{-1}). Heavy rainfall and high baseflow thus combined to produce a rapid increase in streamflow (Figure 4), with two successive waves between 11:00 and 13:00, and between 15:00 and 18:00 on 3 August. Generally, bedload transport followed the same trend as streamflow, with two larger waves taking place with a comparable timing to streamflow peaks on 3 August.

The 3 August 2020 bedload transport event (return period ~1–2 years) was the largest one recorded during the year 2020 at the outlet monitoring station, with a peak water depth of 0.39 m (corresponding to a streamflow of 4.3 m^3 s^{-1}), and a peak of bedload transport of 1,240 kg min^{-1} measured simultaneously (~12:15). Over its duration (Figure 4), ~74,000 kg of coarse material export were estimated at the outlet according to the SPG recording, which represents ~11% of the coarse material that was transported over the year 2020 (Antoniazza et al., 2022). In comparison to the period 2016–2020 analyzed by Antoniazza et al. (2022), the 3 August 2020 event is the fifth largest in terms of bedload transport rate peak, the largest being monitored on 6 August 2018, with a bedload transport rate peak measured at 3,540 kg min^{-1}.

3.2. Seismic Model Parameterization and Seismic-SPG Comparison

At the seismic sensor located close to the SPG monitoring station, the RTK-dGPS survey combined with GIS measurements gave a channel width of $W = 6$ m, a channel gradient $\theta = 0.1$ radians, and a distance between the seismic

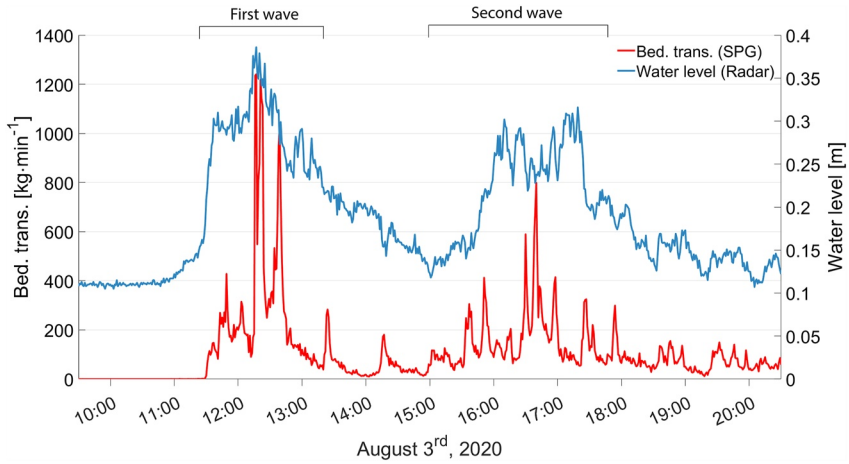

Figure 4. The 3 August 2020 bedload transport event measured at the Vallon de Nant outlet monitoring station. Bedload transport time-series measured with the 10 calibrated Swiss Plate Geophone units is plotted (in red) together with the radar-based water level time-series (in blue).

sensor and the river centerline $r_0 = 5$ m. The application of a best-fit log-raised cosine function to a line-by-number count of riverbed mobile material gave $D_{50} = 0.06$ m, and $\sigma_g = 0.9$, with an RMSE of ± 0.8 m^{-1} (Figure 5a).

Data from the active experiment were then used to derive the seismic ground property parameters v_{p0}, ξ, K, and η in Equations 1a–1c. The decay in wave group velocity with frequency between the two seismic loggers spaced

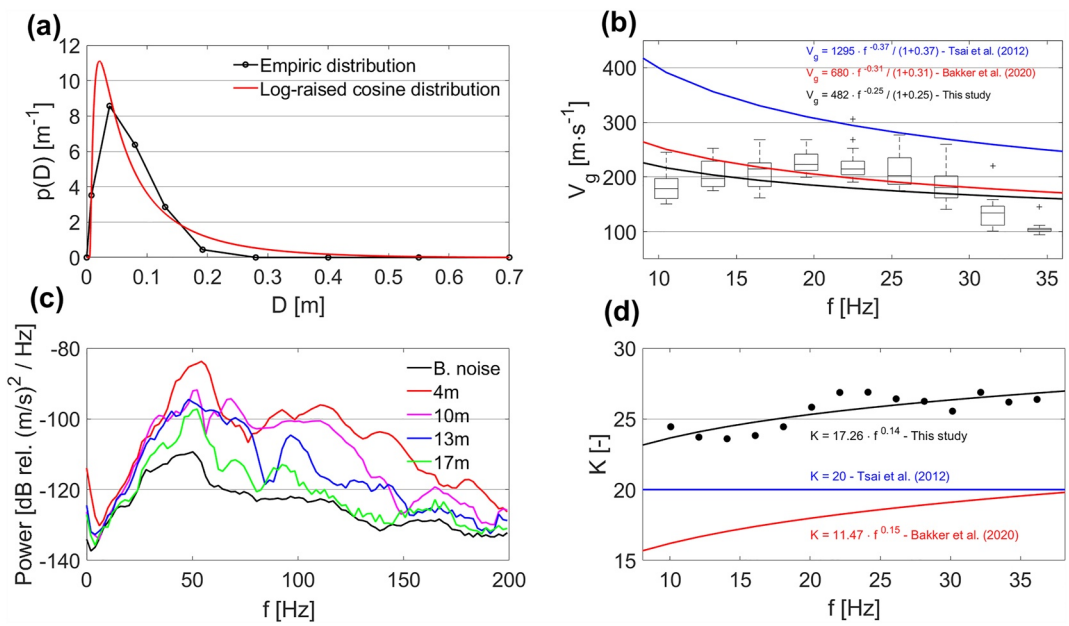

Figure 5. Parameter estimate for the seismic sensor S1 located close to the Swiss Plate Geophone monitoring station (see also Figure 1a). In panel (a), best-fit log-raised cosine function applied to a line-by-number count of 100 mobile particles of the bed, to derive parameters D_{50} and σ_g (RMSE = ± 0.8 m^{-1}). In panel (b), decay in wave group velocity with frequency between two seismic sensors located on opposite banks. The boxplots show the variability for 20 repeated impacts with a sledgehammer. The regression curve (black) describes the wave group velocity decay with frequency (RMSE = ± 35 m·s^{-1}), based on Equations 1a and 1b, and the parameters found by Bakker et al. (2020) for an alluvial channel (in red), and proposed by Tsai et al. (2012) for a generic bedrock site (in blue), are presented for comparative purpose. In panel (c), attenuation of seismic power with distance. Lines represent the average of 20 repeated impacts using a sledgehammer (i.e., without including pauses between sledgehammer blows), and the line in black shows the background noise of periods without active seismic experiment. In panel (d), change in the quality factor K with frequency according to Equation 1c (RMSE = ± 1.4). The parameters found by Bakker et al. (2020) for an alluvial channel (in red), and proposed by Tsai et al. (2012) for a generic bedrock site (in blue) are presented for comparative purpose.

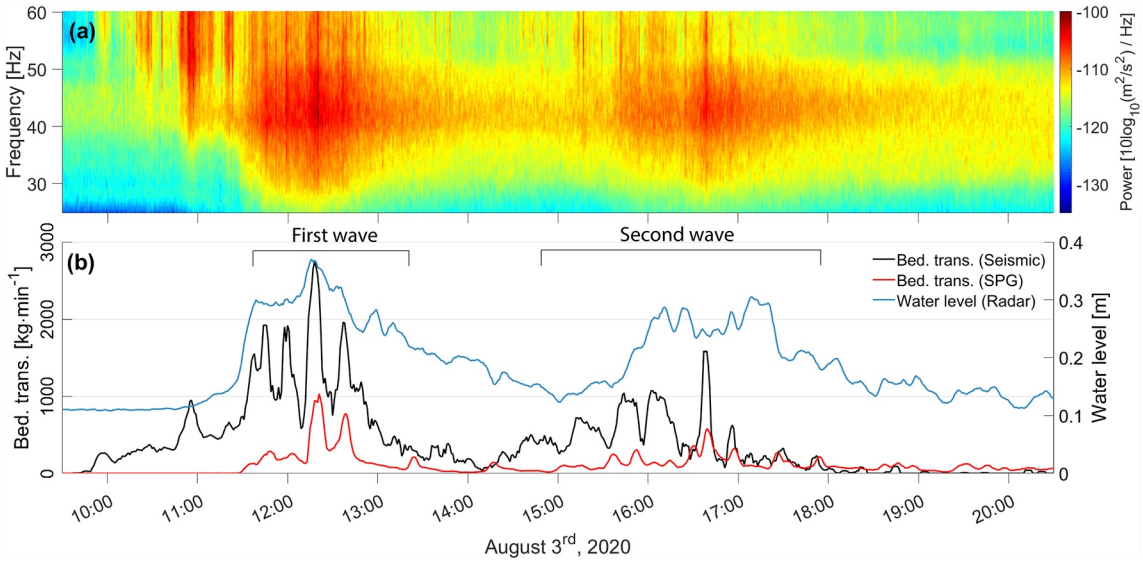

Figure 6. In panel (a), seismic power spectrogram of the 3 August 2020 bedload transport event for the seismic sensor S1 located close (~20 m) to the Swiss Plate Geophone (SPG) monitoring station. In panel (b), time-varying bedload transport estimates (in black) inverted using the Fluvial Model Inversion and the nine parameters constrained locally in the field. The bedload transport time-series derived from the SPG monitoring station is also provided (in red) for evaluation purposes, as well as the water level time-series monitored with the radar-based stage sensor (in blue). Note that a 5-min moving average has been applied to all three time-series.

12 m away on opposite banks was found to be best expressed with $\upsilon_{p0} = 482$ m s^{-1} and $\xi = 0.25$, with an RMSE of ± 35 m s^{-1} (Figure 5b), by combining Equations 1b and 1c. These values are close to, though a bit lower, than the ones found by Bakker et al. (2020) for a similar active seismic experiment conducted in an alluvial channel; but substantially lower than the ones proposed by Tsai et al. (2012) for a generic bedrock site (Figure 5b). Seismic power rapidly decreased with distance at the different frequencies toward background signal level (Figure 5c). Change in the quality factor K with frequency was estimated using Equation 1c, and gave $K_0 = 17.3$ and $\eta = 0.14$, with an RMSE of ± 1.4 (Figure 5d). The frequency dependency of K is not very strong, which is consistent with the constant value of $K = 20$ proposed by Tsai et al. (2012). The value of the exponent $\eta = 0.14$ is also close to the one found in Bakker et al. (2020) for an alluvial channel ($\eta = 0.15$, Figure 5d).

Following the field-based estimate of the nine parameters in the FMI, the time-varying estimates of bedload transport were inverted (Figure 6). The 3 August 2020 bedload transport event is well visible on the seismic power spectrogram (Figure 6a), with two consecutive periods (11:00–13:00 and 15:00–18:00) recording substantially more seismic energy (i.e., >-110 dB) than the preceding (09:30–11:00), interceding (13:00–15:00) or following (18:00–20:30) ones. In Figure 6b, the results of the bedload transport seismic inversion are presented (in black), together with the time-series of bedload transport (SPG monitoring, in red) and of water depth (radar monitoring, in blue). Results of the inversion show that the seismic-based estimates of bedload transport vary together with changes in the seismic power, with bedload transport rate being low during periods of weak seismic energy and peaking up to ~2,700 kg min^{-1} at its maximum (12:18).

The general trend of the bedload transport event sensed with the SPG monitoring system is identified by the bedload seismic inversion (Figure 6b). On 3 August 2020, both monitoring systems estimated a first wave with greater magnitude at 11:00–13:00, and a second with smaller magnitude at 15:00–18:00. Outside of these periods of high bedload activity, both monitoring systems sensed no or little bedload transport (e.g., 18:00–20:30). The timing of the greater bedload transport peaks (seismic-inverted bedload transport >1,000 kg min^{-1}) is relatively synchronous for both monitoring systems: there are 3 min of lag in the peak of the first major bedload transport wave (~12:15), and 1 min of lag in the peak of the second major bedload transport wave (~16:40), while both waves last multiple hours. For the second major bedload wave (16:00–18:00), the radar-based water level sensor detects multiple high peaks in streamflow, while both bedload transport monitoring systems estimated a higher transport peak occurring in-between in a period of relatively lower streamflow (at ~16:40). This suggests in this

instance that the FMI is indeed able, based on different frequency bands, to differentiate between seismic sources related to either flowing water or bedload transport, and that inverted bedload transport is not only a function of increasing water depth and increasing turbulence rate.

The seismic inversion of bedload transport generally tends to overestimate the SPG-derived bedload fluxes, to a factor of 4 on average for bedload transport rates greater than 60 kg min^{-1} (1 kg s^{-1}). Over the duration of the bedload transport event, ~50% of the 1-min data points are below a factor 3 of difference, and the two previously identified bedload transport peaks (~12:15 and ~16:40) both present a factor 2.7 of difference. At the beginning of the event (10:00–11:30), the seismic-inverted bedload estimates rise progressively with bursts, while the SPG monitoring derives no bedload transport. In the tail of the event (>18:00), the SPG estimates more bedload transport than the seismic inversion does. Over the duration of the bedload transport event (Figure 6b), the seismic inversion of bedload transport gives a total transported mass of $\sim 2.8 \times 10^5$ kg, on average a factor 3.8 of difference (~74% greater) compared to the $\sim 0.74 \times 10^5$ kg estimated by the SPG system. Note that the seismic-inverted bedload transport estimates are close to zero before (<9:30) and after (>20:00) the event occurrence.

3.3. Spatially Distributed Time-Varying Bedload Transport Estimates

The seismic power spectrograms of every sensor (columns 1 and 3 in Figure 7) show more seismic energy recorded on 3 August between 11:00 and 18:00, as compared to preceding and following periods. In most instances, two distinct periods of higher seismic energy (11:00–13:00 and 15:00–18:00) corresponding to the two bedload waves identified in Figure 6, are observable (e.g., S1, S3, S5, S6, S7, S8, etc.). Sensors close to the continuously flowing main channel (e.g., S1, S2, S3, S5, S7, S8, S10) tend to record more seismic energy throughout the period due to permanent turbulence, as compared to temporally flowing tributaries (e.g., S4, S6, S9, S15, S19), which only show higher seismic energy during discrete hydrological events. Seismic power spectrograms may not be directly comparable to each other due to site-specific differences (e.g., ground seismic properties, distance to seismic source), which are not yet taken into account at this stage of the processing. For instance, sensor S12, located along the main channel, seems to record relatively little seismic energy, but this is likely because it was positioned relatively far (~30 m) from the flow.

Figure 7 (columns 2 and 4) shows the results of seismic inversion. The two bedload waves identified in Figure 6 at sensor S1 are visible—with differences in timing and magnitude at S2, S3, S7, S8, and S10 (upper limit of the semi-alluvial Reach 4 in Figure 1b). From S10 on, it becomes harder to track the bedload waves since the main channel is now fed by multiple tributaries draining relatively large sub-catchments (Figure 1a). The two waves are nevertheless visible at S12, S13, S14, S16, S17, S21, and S22. While large bedload waves were inverted in some tributaries (e.g., S4, S6, S11, S16, S17), no or little bedload transport was estimated within others (e.g., S9, S15, S19). Although no bedload transport was inverted for S9 and S15, higher seismic energy is visible at the timing of the bedload transport event. As its frequency was outside of the bedload-specific bands, this is likely related to passage of a bedload-free water wave.

The time-varying estimates of bedload transport are arbitrarily combined into hydrological sub-catchments (1–6) in Figures 8 and 9a, to help the visualization of the bedload transport event downstream propagation. From Figure 8, we can note that inverted bedload transport estimates start from a zero level before the event occurrence. Most of them go back to zero after the event (e.g., S1, S2, S3, S4, S8, S20), while remanent seismic energy inverted residual bedload transport in some instances (e.g., S16, S17, S22). We can also see general coherency in bedload transport patterns (e.g., shape, timing, magnitude) inverted from spatially consecutive seismic sensors, for instance within sub-catchments (3), (4), and (6). But tributary inputs may show quite different behaviors as compared to the coarse material transported into the main channel they feed, for instance S5 in sub-catchment (1).

The estimated mass of coarse material transported over the duration of the event is presented in Figure 9a. Starting from upstream, large amounts of bedload (>~10^6 kg) were inverted from sub-catchments (4, 6), in particular at sensors S16, S17, and S21. In contrast, substantially less bedload (~10^5–5×10^5 kg) was estimated through sub-catchment (5), which drains the upper watershed area (i.e., where the glacier lies; Reach 1 in Figure 1b). In sub-catchment (4), the large amount of bedload (>~10^6 kg) inverted at S21 and S17 seem to be already substantially attenuated (i.e., deposition occurred) at S14 (~10^5–5×10^5 kg). In sub-catchment (5), coarse material is supplied from three different tributaries, and relatively less bedload is transported downstream of their confluence at S18. In sub-catchment (6), bedload transport increases from S20 (~5×10^5–10^6) to S17 (>~10^6 kg), before decreasing at S13 (~5×10^5–10^6 kg), with no tributary input from S15. In sub-catchment (3),

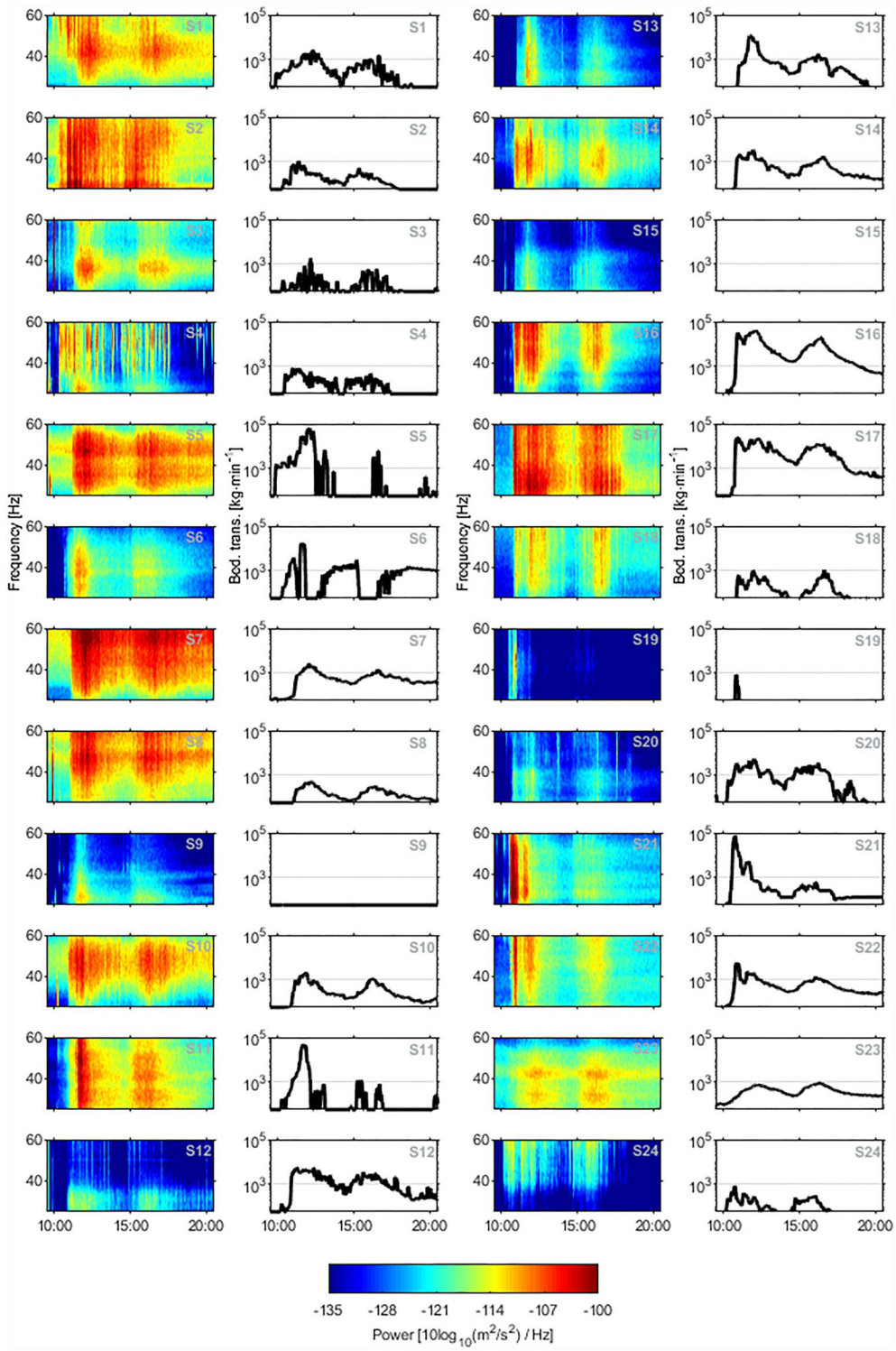

Figure 7. Seismic power spectrograms and seismic-inverted time-varying bedload transport estimates for the 24 seismic sensors distributed in the Vallon de Nant Alpine watershed. The inversion focuses on the bedload transport event that took place on 3 August 2020. The seismic sensors are labeled S1–S24 from downstream (the Swiss Plate Geophone monitoring station) to upstream (Figure 1a). Note the *y*-axis log-scale, and that a 5-min moving average has been applied to time-varying estimates of bedload transport.

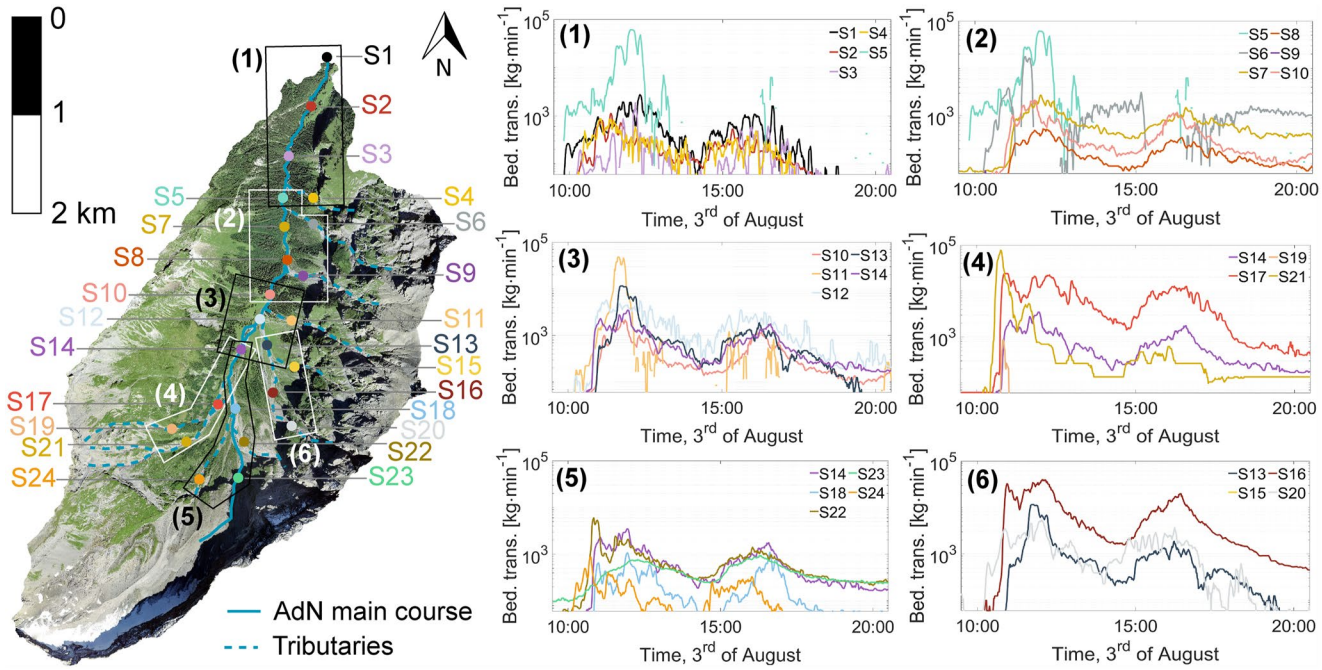

Figure 8. Time-varying bedload transport estimates on 3 August 2020 (09:30–20:30) for the 24 seismic sensors deployed in the Vallon de Nant Alpine watershed. The dots represent the location of the seismic sensors and their color corresponds to the color of the inverted bedload transport time-series in the graphs to the right. Time-varying estimates of bedload transport are arbitrarily combined into sub-catchment groups (1–6) to better visualize how coarse material moves through the watershed. Note that a 5-min moving average has been applied to inverted time-series of bedload transport. Acknowledgments ©Swisstopo.

larger amounts of bedload are estimated at S13 ($\sim 5 \times 10^5$–10^6 kg) supplied from sub-catchment (6), than there are at S14 ($\sim 10^5$–5×10^5 kg) supplied from sub-catchments (4) and (5) combined. There is still a substantial amount of bedload estimated at S12 ($\sim 5 \times 10^5$–10^6 kg), which drains all sub-catchments (4), (5), and (6). Although bedload transport at S12 combines with a significant tributary input coming from S11 ($>\sim 10^6$ kg), substantially less bedload is estimated at S10 ($\sim 10^5$–5×10^5 kg) at the downstream end of sub-catchment (3), which also corresponds to the end of the braided river reach (Reach 3 in Figure 1b).

Compared to tributary inputs in the upper watershed (e.g., S21, S17, S11), there is progressively less bedload estimated in the main channel throughout sub-catchment (2), where different sensors (S10, S8, S7) suggested between $\sim 10^4$ and $\sim 5 \times 10^5$ kg of material. Heading downstream over consecutive sensors, there is relatively more bedload material measured at S10, less at S8 and more again at S7, with no tributary input from S9, which suggests that erosion also takes place. There is another substantial tributary estimated supply at S6 ($\sim 5 \times 10^5$–10^6 kg), which combines with estimated supply from S7 in the main channel ($\sim 10^5$–5×10^5 kg) to translate into an important bedload flux inverted at S5 in the main channel ($>\sim 10^6$ kg). This high magnitude estimate sediment flux rapidly attenuates (i.e., deposition occurs) throughout sub-catchment (1), where $\sim 10^4$–5×10^5 kg of material are estimated over the different sensors (S1, S2, S3). Again, a relatively greater mass of bedload transport is estimated at S1 and S2 as compared to S3 located upstream, which suggests the occurrence of erosion.

If we take within each headwater tributary the sensor that has the greatest estimated mass of transported material over the duration of the event (i.e., sensors S4, S6, S11, S16, S17, S22, S23, and S24), and sum their respective mass, we can approximate a minimum of $\sim 1.1 \times 10^7$ kg of bedload material mobilized in the headwater channels during the 3 August 2020 bedload transport event. In comparison, only $\sim 2.8 \times 10^5$ kg is estimated to be exported at the outlet (sensor S1), which represents ~2.5% of what has been mobilized. This is a minimal estimate, since it assumes that only deposition took place downstream of the headwater sensors, while evidence of erosion (greater bedload mass at downstream sensors compared to upstream ones) was also observed (e.g., between S8 and S7, between S3 and S2). In addition, we do not know if the bedload material estimated at two consecutive sensors is the same, and in what proportion, or whether deposition and erosion also occurs in-between sensors. Thus, it is likely that an even lower proportion of the approximated total amount of coarse material mobilized through the watershed is actually exported at the outlet.

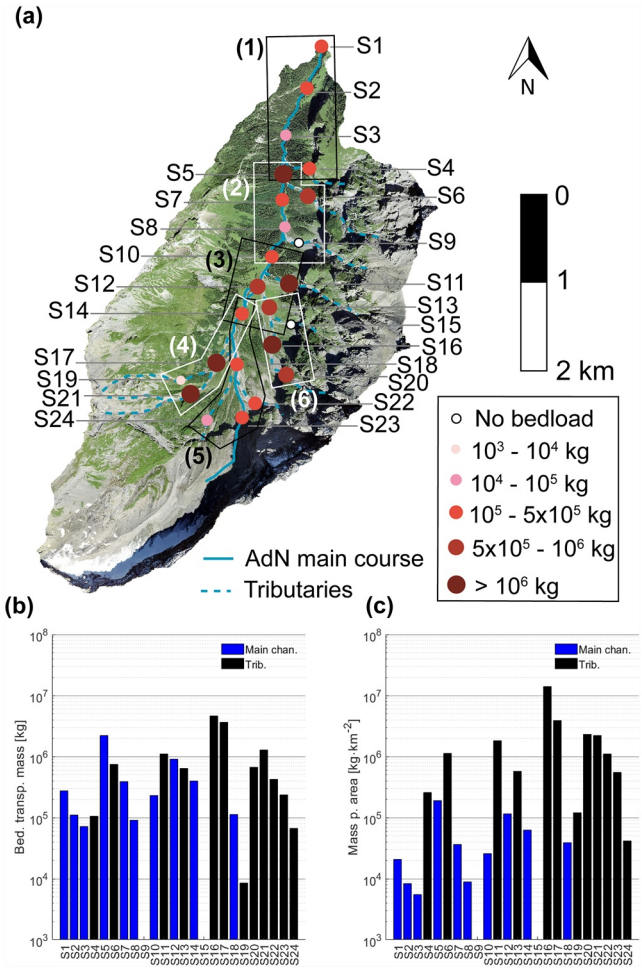

Figure 9. In panel (a), mass of bedload transport estimated over the duration of the 3 August 2020 bedload transport event in the Vallon de Nant Alpine watershed, at the 24 locations where a seismic sensor was deployed. Inverted time-series of bedload transport are arbitrarily combined into sub-catchment groups (1–6) to better visualize how coarse material moves through the watershed. In panels (b, c) respectively, bedload transport mass and bedload transport mass per unit area estimated at each of the 24 seismic sensor location, in the main channel (in blue) and in the tributaries (in black). Acknowledgments ©Swisstopo.

The estimated bedload mass transported over the duration of the event and the estimated transported bedload mass per unit area at each of the 24 seismic sensor locations are presented in Figures 9b and 9c, respectively. The data presented in Figures 9b and 9c are available in Text S5 in Supporting Information S1.

As observed in Figures 8 and 9a, both the estimated bedload transport mass (Figure 9b) and the estimated bedload transport mass per unit area (Figure 9c) tend to be greater in the steep tributaries (e.g., S4, S6, S11, S16, S17) as compared to the AdN main channel (e.g., S1, S2, S3, S7, S8, S10). It suggests a strong filtering of the bedload transport signal between the headwater tributaries and the watershed outlet on the one hand, and an inversely proportional relationship between contributing area and the estimated bedload transport mass on the other hand. The trend of attenuation in the bedload transport signal (i.e., occurrence of deposition) in the downstream direction is however sometimes complex due to high rates of material supply from tributaries into the main channel (e.g., S6 → S5), which may also not always be synchronous with bedload transport waves in the main channel.

3.4. Spatially Distributed Bedload Transport Timing

The start and end of bedload transport (blue circles) and the timing of the major bedload transport waves (red circles) at each seismic sensor location are presented in Figure 10a. Starting from upstream, the bedload transport event is estimated to begin relatively synchronously on the headwater tributaries (S19–S24), at ~10:00 on 3 August. The timing of the major bedload waves suggests an earlier activity in sub-catchment (4) at S19 (i.e., one wave at 10:54) and S21 (i.e., two waves at 10:49 and 14:55), as compared to sub-catchment (6) (i.e., two waves at 11:44 and 15:44). The different headwater tributaries in sub-catchment (5) show a substantial variability in the timing of the bedload transporting event, with the two waves occurring earlier at S24 (i.e., 11:15 and 15:34), then at S22 (i.e., 11:32, 16:21), and finally at S23 (i.e., 12:24 and 16:39). The tracking of the bedload transport event downstream from headwater tributaries is made more complex by the multiple tributaries transporting different amounts of sediment at different times, over river reaches of different lengths and with different transport efficiency. A general lag in downstream direction (decreasing from S24) in the timing of the bedload starting point, and in the timing of the two major bedload waves, is observable in Figure 10a, notably in the upper part of the watershed (sensors S24–S7).

Figure 10b presents the inter-sensor distance (m) (up left), the lag between two consecutive inverted bedload transport time-series (min) (up right), the maximum r-values (–) corresponding to that lag (bottom left), and the associated propagation velocity (m min^{-1}) (bottom right). The data in Figure 10b are available in Text S6 in Supporting Information S1. Cross-correlation analysis suggests a rapid propagation of the bedload transport event through sub-catchment (d), with estimated velocities of 97 m min^{-1} between S19 and S17 (r = 0.35) and of 28 m min^{-1} between S21 and S17 (r = 0.48). The bedload transporting event also propagates rapidly through sub-catchment (6), with an estimated velocity of 57 m min^{-1} between S20 and S16 (r = 0.89). In sub-catchment (5), smaller propagation velocities (10 m min^{-1}) were estimated from S24 to S18 (r = 0.78), and higher ones (41 m min^{-1}) between S22 to S18 (r = 0.72). The bedload transport event occurs almost synchronously at S18 and at S23 (Figure 10a), whilst they are located 651 m away. Either S18 is first supplied by S24 and S22 which showed an earlier activity, or local hydrological and sediment availability conditions generate a mobilization that may be, at least partly, independent from the upstream event propagation.

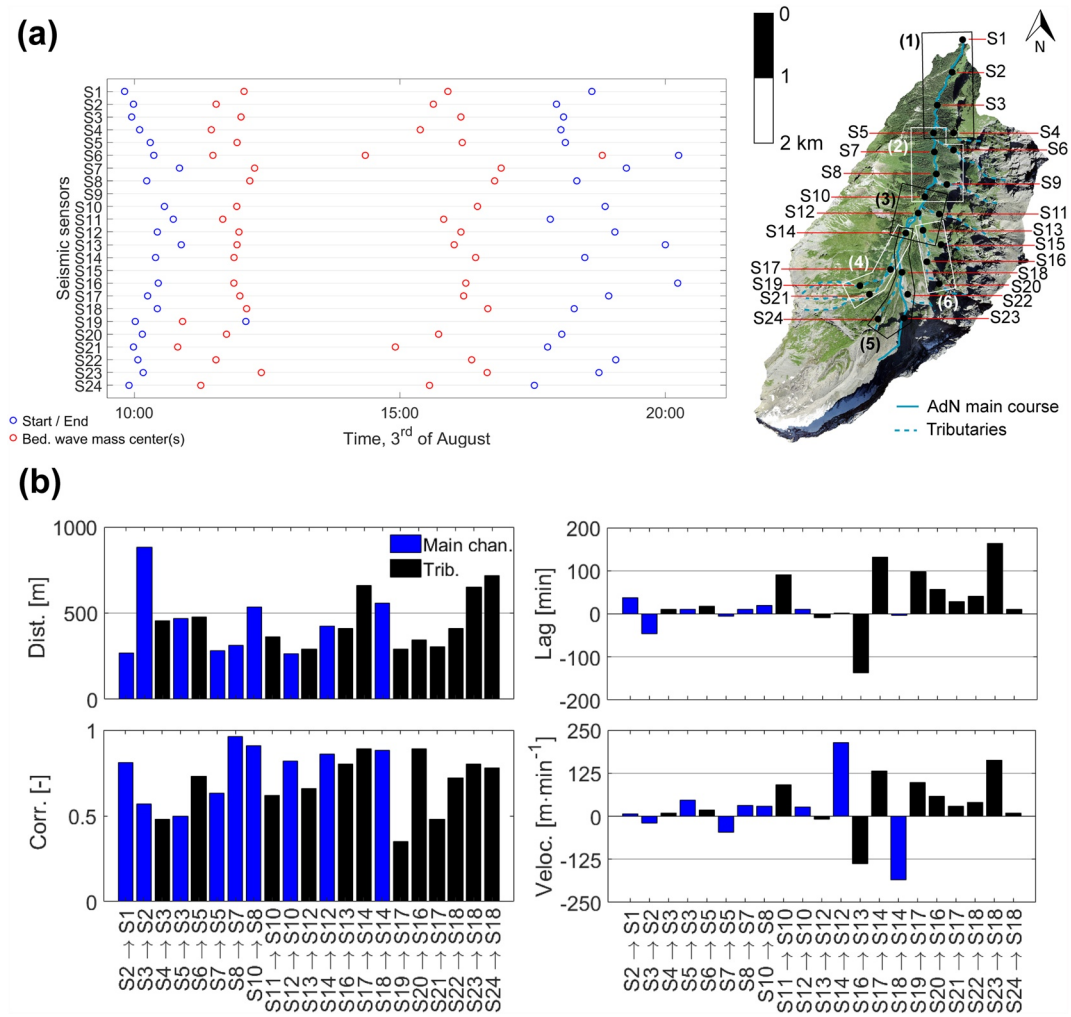

Figure 10. In panel (a), start and end of the bedload transporting event (blue circles) and timing the major bedload transport waves (red circles) estimated at the 24 seismic sensor locations, from upstream (S24) to downstream (S1). Note that the downstream propagation of the major bedload transport waves in the main channel is turned complex by tributary inputs (e.g., S5, S19), which may be active at different timing than bedload transport waves in the main channel. In panel (b), inter-sensor distance (m) (top left), estimated lag (min) between time-series of bedload transport inverted from two spatially consecutive seismic sensors (top right), and associated correlation *r*-values (*r*) (bottom left), as well as estimated bedload transport velocity (m min^{-1}) between sensor pairs (bottom right). Acknowledgments ©Swisstopo.

The bedload transporting event appears to propagate very rapidly between S17 and S14 (132 m min^{-1}, $r = 0.89$), which also raises the question whether a spatially continuous propagation of the event from upstream is reasonable. A later activity at S18 as compared to S17 and S14 suggests that S14 at the downstream end of sub-catchment (d) is first supplied by S17, and later by S18, which may explain the negative velocity measured between S14 and S18. In the downstream part of sub-catchment (e), the bedload transport event is estimated to occur almost simultaneously at both S16 and S13, while they are located 411 m away. The same observation is to be made for sensor pairs S12 and S14, where a short 2-min lag has been estimated between sensors spaced 426 m away, which may also explain the negative velocity measured between S12 and S13. A 10-min lag is estimated between S10 and S12 spaced 263 m away, which turns into a velocity of 26 m min^{-1} ($r = 0.82$). S10 is also fed by a tributary input from S11, which shows a high velocity 91 m min^{-1} ($r = 0.62$). Earlier activity at S11 suggests that S10 may be first supplied by the tributary, and shortly after by S12 in the main channel (Figure 10a). The propagation of the bedload transport event downstream from S10 to S8 and S7, shows a clear consistency, with velocities of 28 ($r = 0.91$) and 31 m min^{-1} ($r = 0.96$), respectively. A negative velocity is then measured between S5 and S7, and is likely related to an earlier activity in tributary S6, which supplies material to S5 (18 m min^{-1}, $r = 0.73$)

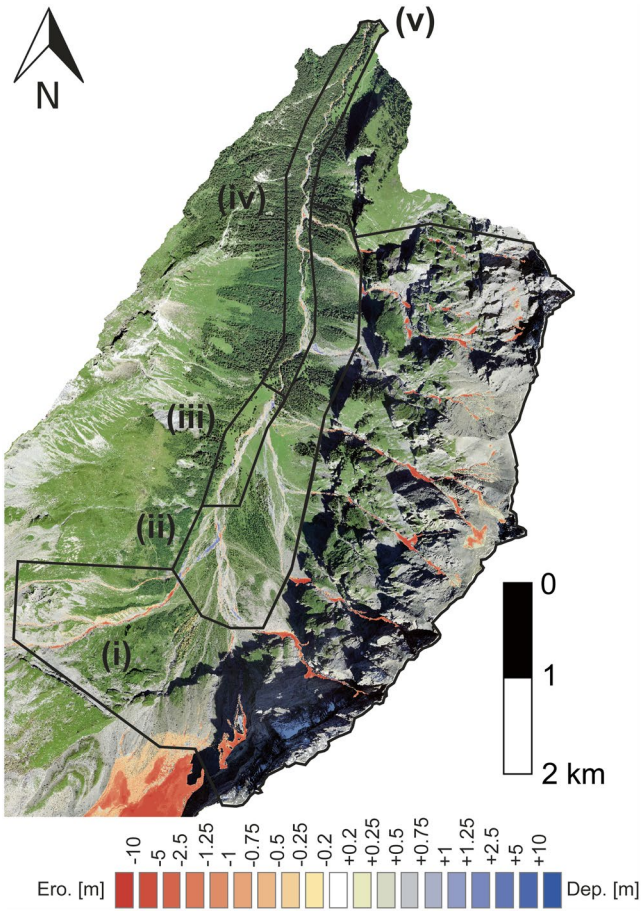

Figure 11. Morphological change (erosion and deposition) estimated through digital elevation models differencing between two 0.5-m resolution LIDAR-based SwissAlti3d models of 2016 and 2020, over an orthophoto of 2020. Acknowledgments ©Swisstopo.

before the bedload transport from the main channel at S7 makes it to S5. A similar early supply from tributary S4 to S3 (10 m min^{-1}, $r = 0.5$) in the main channel suggests that S3 is first supplied by the tributary input from S4, and later on by material from the main channel at S5. Sensor S2 shows an earlier activity than sensors located upstream from it, which results in a negative propagation velocity, and also questions the likelihood of a spatially continuous downstream propagation. Downstream propagation from S2 to S1 results in a velocity of 7 m min^{-1} ($r = 0.81$).

3.5. Longer-Term Morphological Change Analysis

Morphological change during the period 2016–2020 are presented in Figure 11. We computed sediment budgets (Table 1) for different geomorphological zones (i.e., tributaries, alluvial fans, braided channels, semi-alluvial channels) to emphasize their respective contribution to the watershed sediment budget. Note that the "zone" categorization used here is different than the "sub-catchment" categorization defined in Section 3.3. This is because the goal of the "sub-catchment" categorization was to observe the propagation of bedload transport waves within a same channel across different geomorphological zones of the watershed (e.g., from a tributary to an alluvial fan to a braided reach), while the goal of the "zone" categorization is to compute sediment budgets within different geomorphological zones of the watershed.

In Figure 11, melt and subsidence of the glacier tongue in the upper watershed is observable (i.e., not accounted in volume change estimates to only focus on fluvial erosion and deposition). Substantial erosion is visible in a number of steep gullies feeding the tributaries, notably upstream of S4, S6, S9, S11, S15, S21, and S22. Patches of erosion with substantial depths (i.e., meters) are visible high up in the rockwalls, notably on the eastern face of the VdN Alpine watershed. In this tributary-dominated area (zone "i" in Figure 11 and Table 1), ~5.435 × 10^5 (m^3) of material were eroded during the period 2016–2020, which represents ~96% of the total volumetric erosion estimated across the whole watershed over the same period. Substantial deposition also took place in this area (~0.484 × 10^5 (m^3)), which represents ~55% of the total volumetric deposition estimated across the watershed over the period 2016–2020. Thus, erosion remains largely dominant (~92%) with respect to deposition, and ~4.951 × 10^5 (m^3) of material are estimated to have been exported from the tributary-dominated zone, confirming the tributaries as likely primary sources of coarse material during bedload transport events such as the one monitored on 3 August 2020. Over the alluvial fan surfaces at the downstream gully margins (zone "ii" in Figure 11 and Table 1), morphological change tends to be dominated by deposition (~69% of total volume change). Patches of deposition with substantial depths (i.e., meters) notably occurred downstream of S17, downstream of S22, and to a lower extent downstream of S16.

Table 1
Erosion and Deposition Volumes Estimated Through Digital Elevation Models Differencing Over the Period 2016–2020 (Numbers Associated to Figure 11)

Zone	Erosion (×10^5 m^3) (volume, percentage)	Deposition (×10^5 m^3) (volume, percentage)	Percentage erosion versus cumulative change (%)	Net balance (×10^5 m^3)
(i) Tributaries	−5.435, 96%	+0.484, 55%	92	−4.951
(ii) Alluvial fans	−0.141, 2.5%	+0.313, 35%	31	+0.172
(iii) Braided reach	−0.03, 0.5%	+0.05, 5.5%	38	+0.02
(iv) Semi-alluvial reach	−0.05, 1%	+0.04, 4.5%	56	−0.01
(v) Whole watershed	−5.656, 100%	+0.887, 100%	86	−4.769

Another zone of deposition is visible on the alluvial fan downstream of S11, at the confluence with the AdN main channel close to S10. Other depositional zones in similar settings (i.e., over the surface of alluvial fans, or at their feet close to the confluence with the AdN main channel) are visible downstream of S9, S6, and S4. About ∼35% of the deposition measured over the whole watershed occurs in this alluvial fan-dominated zone. In contrast, erosion is negligible (∼2.5% of the erosion measured over the whole watershed), and a net deposition of $\sim 0.172 \times 10^5$ m^3 is estimated in this zone over the period 2016–2020.

Along the braided channel reach (zone "iii" in Figure 11 and Table 1), deposition is also largely dominant with respect to erosion (∼62%), notably around S14, S12, and S10; and ∼5.5% of the deposition estimated across the whole watershed takes place in this zone. Erosion is again negligible (∼0.5% of the erosion estimated over the whole watershed), and a net deposition of $\sim 0.02 \times 10^5$ (m^3) is derived within it over the period 2016–2020. Many areas of the braided channel zone "iii" also have no detectable change. Along the semi-alluvial reach (zone "iv" in Figure 11 and Table 1), morphological changes tend to alternate between shallow patches of both erosion and deposition, with many areas also presenting changeless surfaces. Erosion slightly dominates the sediment budget (∼56%), and a net balance of $\sim -0.01 \times 10^5$ (m^3) is derived, but both erosion and deposition volumes estimated in zone "iv" represent relatively small proportions with regards to the ones inferred for the whole watershed (∼1% and ∼4.5%, respectively). Over the whole watershed (v), erosion dominates the sediment budget (∼86%), with a net export of $\sim 4.769 \times 10^5$ m^3.

4. Discussion

4.1. Evaluation of the Seismic Inversion Approach

The two major bedload waves monitored by the SPG system (Figure 4) were both detected in the seismic-inverted time-varying estimates (Figure 6). Over the duration of the investigated bedload transport event, the estimated transport rates (kg min^{-1}) from the seismic monitoring tended to be higher, on average by a factor of 4, than the bedload transport rates derived from the calibrated SPG system for transport rates greater than 60 kg min^{-1} (1 kg s^{-1}). The difference was lower for the peaks of the two major bedload waves identified in Figure 6b (factor 2.7 of difference). This result is positive and gives some confidence in the performance of the FMI since all required parameters were determine beforehand in the field, the inversion was constrained without using measured data, and the seismic-inverted time-series was not adjusted by any empirical factor to better fit the SPG data. Given the low cost, ease-of-deployment and ease-of-maintenance of seismometers (Bakker et al., 2020; K. L. Cook & Dietze, 2022; K. L. Cook et al., 2018; Dietze et al., 2022a, 2022b), seismic data collected at sensor S1 results in a relatively reliable time-varying estimate of bedload transport, at a factor 100 cheaper than the SPG monitoring for the VdN case. The performance of the seismic inversion approach at S1 is also substantially better than outcomes from capacity-based bedload transport equations in this environment, with at least an order of magnitude of error typically reported (Ancey, 2020a, 2020b; Recking, 2013; Schneider et al., 2015; Yager et al., 2015), and roughly two orders of magnitude for daily bedload transport predictions in the specific VdN case (Antoniazza et al., 2022). A range of reasons can be invoked to explain the residual difference between the SPG and the seismic-inverted time-series at S1. It may be related to errors in the seismic model (i.e., observations also valid for the other deployed seismometers), but also from errors in the SPG monitoring.

In terms of the seismic model, uncertainty in seismic inversion of bedload fluxes is possible because of frequency overlaps between the bedload transport signal (∼20–60 Hz) and the low-frequency (∼1–20 Hz) turbulence signal (Bakker et al., 2020; Dietze et al., 2019, 2022a; Gimbert et al., 2014, 2019). The presence of a step (∼1 m high) at the SPG weir (Figure 2a) may generate turbulence that contaminate the bedload-specific frequency bands used in the FMI (Schmandt et al., 2013, 2017), leading to overestimation of the inverted bedload transport rates. This hypothesis is not the most likely in our setting because the inversion frequency band used in this study (25–60 Hz) was chosen to minimize the risk of signal contamination by turbulence (<20 Hz, Gimbert et al., 2014). In addition, seismometers were located relatively close to the stream (∼5–30 m) and former research has shown that seismic energy related to bedload transport tends to outweigh the signature of river turbulence in the frequency band specific to bedload transport (Bakker et al., 2020; K. L. Cook & Dietze, 2022). This assertion can be verified by looking at the mean empirical spectra measured by the 24 seismometers in Text S4 in Supporting Information S1. In Figure 6, we were able to identify peaks in bedload transport rates synchronous with peaks measured with the SPG system, independently from peaks in water depths (as a proxy of turbulence rate), giving confidence in this instance in the capacity of the FMI to partition between turbulence and bedload transport seismic signal. Water depth being easily measurable using stage sensors (Antoniazza et al., 2022; Nicollier, Antoniazza, Ammann,

et al., 2022) or pressure sensors (Comiti et al., 2019; Dell'Agnese et al., 2015), further research should investigate how much improvement FMI is achievable if exact measurements of water depths are used to drive the inversion.

Second, it was shown that high-frequency seismic noise (typically >80 Hz) induced by rainfall drops may also overlap with bedload-specific frequency bands (down to ~40 Hz, Bakker et al., 2022), with substantial energy released (up to ~140 dB), which may contaminate the inversion of bedload transport. This may be an explanation for the earlier onset of bedload transport inverted from the FMI as compared to the SPG recording, with strong seismic power recorded into high frequencies (>45 Hz) in Figure 6 between 10:00 and 11:00. However, the fact that low levels of seismic noise and bedload transport were detected at seismic stations subject to the same rainfall event (S9, S15, Figures 7 and 8) thus suggests that rainfall effect may not always be significant. Further research should investigate how to better isolate seismic sensors from the effect of rainfall (e.g., deeper burial depth, distance from trees producing large drops, sheltering) when performing seismic monitoring of rivers, especially because rainfall and flooding events are often synchronous.

Third, field estimates of the nine parameters needed to constrain FMI are also subject to uncertainty. A Monte Carlo simulation was run (Text S7 in Supporting Information S1) on the FMI model parameters (Dietze et al., 2022b) for seismic sensor S1 located nearby the SPG monitoring station, to assess possible changes in bedload transport estimates with changing model parameters. The first three runs (500 random combinations each) investigated the effect of channel width W, of the GSD parameters (D_{50} and σ_g), and of the ground seismic property parameters (v_{p0}, ξ, K_0, and η), on the FMI model outputs. The fourth run made all those parameters vary simultaneously (1,000 random combinations). The range picked for each parameter was chosen according to their expected precision estimated at S1 (Text S7 in Supporting Information S1). Results of the Monte Carlo simulations suggest that the relative shape of the inverted bedload transport event is generally maintained with variations in channel width, GSD parameters or ground seismic properties. Variability in simulation outputs are under one order of magnitude variability as compared to the inverted time-varying bedload transport estimate (Figure 6, Text S7 in Supporting Information S1). When varying all parameters simultaneously, the relative shape of the event is still maintained for most of the simulations, and variability in absolute bedload transport magnitude reaches one order of magnitude. Results of the Monte Carlo analysis (Text S7 in Supporting Information S1) are in line with a similar exercise performed by Dietze et al. (2022a). The authors ran Monte Carlo simulations using random combinations of the nine parameters of the FMI picked within their own plausible range, and showed that inverted transport rates also varied to some extent (within an order of magnitude) between the different simulations. For all runs (Text S7 in Supporting Information S1), the uncertainty is greater in periods of low bedload transport estimates, at the onset of the event (i.e., <10:30), in between the two bedload transport waves (i.e., 13:30–14:30) and at the tail of the event (>18:00), than during periods of higher bedload transport estimates. The fact that the relative shape of the event is mostly maintained in the different runs suggests that the timing of the bedload transport event at the different seismic sensor locations (Figure 10) may be more accurate, while the absolute magnitude of inverted bedload transport time-series is subject to more uncertainty (Figures 7, 8, and 9). Yet, the evidence (Figures 7 and 8) that inverted bedload transport estimates before (<9:30) and after (>20:00) the event are close to zero at the 24 seismic sensor locations suggests that the scaling of the event in absolute magnitude is encouraging. Also, the magnitude of the transport rates we invert along the main channel (e.g., S1, S2, S3, S7, S8) and along some of the steeper reaches (e.g., S6, S13, S22), with instantaneous values up to 10^3–10^4 kg min^{-1}, lies within a comparable range as compared to multiple bedload transport events reported in the literature in similar settings (Comiti et al., 2019; Coviello et al., 2022; Picco et al., 2012; Recking, 2013; Rickenmann, 2001, 2023). The highest inverted instantaneous transport rates, with values up to 8×10^4 kg min^{-1} (e.g., S11, S16, S17, S21), remain within a possible range as compared to transport rates (>1×10^6 kg min^{-1}) reported in the literature for steep (>15%) torrents (McArdell et al., 2023; Schimmel et al., 2022). It should be noted that the nine parameters we used in the inversions were estimated during low flow conditions, while some of them (e.g., width, grain-size) may be changing through time, notably during flood flow conditions, which adds uncertainty (Bakker et al., 2020; Dietze et al., 2022a; Gimbert et al., 2019). For sensor S1, the section was relatively channelized making ground seismic properties and grain-size the likely cause of most uncertainty, but it emphasizes the need for accurate and representative field measurement of the FMI parameters. Further research may help to constraint the best approach to constraint each of them accurately in the field.

Fourth, it should be noted that while the SPG system records bedload fluxes over the surface of the impact plates, seismic sensors may detect turbulence and bedload transport signal up to multiple hundreds of meters away (Bakker et al., 2020; K. L. Cook et al., 2018). It is thus possible that seismic sensors not only record local seismic

energy (i.e., at the cross-section where they are deployed), but integrate seismic energy over a certain length of channel (i.e., in both upstream and downstream directions), which may result in the same bedload transport being measured multiple times. This effect may explain part of the overestimation of the seismic-inverted bedload transport time-series as compared to the SPG measurement, and should be kept closely in mind when retrieving bedload transport estimates from any river seismic monitoring. Also, it could explain why a progressive increase in seismic-inverted bedload transport is observed (Figure 6, 10:00–11:30), while the radar measurement shows no sign of the flood yet, if bedload moving further upstream in the watershed is already detected. The effect of spatial averaging of the seismic signal could also lead to an early determination of the event start, and a late determination of the event end (Figure 10a, blue dots). In contrast, it should neither affect substantially the timing of the major bedload transport waves (Figure 10a, red dots), nor the velocities derived from the cross-correlation analysis (Figure 10b), if we assume that the speeds of the bedload transport waves are constant throughout the period of detection and the spatial averaging in both upstream and downstream directions is symmetric.

But part of the difference between the SPG and the seismic estimate of bedload transport may also be due to errors in the SPG recording. First, the calibration of the SPG system performed in Antoniazza et al. (2022) had a level of explanation of 85%, so part of the variance is not explained by the calibration relationship to which the bedload transport seismic inversion is compared. Second, the fact that over the event duration the total bedload transport mass measured with the SPG system was 74% smaller than that inverted seismically could also reflect the higher particle detection threshold (>10–20 mm) of the SPG system (Antoniazza et al., 2022; Nicollier et al., 2021; Wyss et al., 2016b). Smaller particles (<10–20 mm) may also emit detectable seismic noise if hydraulic and transport conditions allow it. Smaller grains excite higher frequencies, and typically lower amplitudes, because for a given speed their kinetic energy is smaller. As a consequence, the largest grains dominate the seismic energy, as implemented in the physical inversion model (Tsai et al., 2012) and verified also in field experiments (Bakker et al., 2020; Lagarde et al., 2021). In addition, higher frequencies are also attenuated quicker than lower ones. So the minimum detectable grain-size of seismometers depends on all (a) the hydraulic conditions in the river (absolute impact energy of small grains); (b) the bedload GSD (relative impact energy of particles of different sizes); (c) the ground seismic properties and their attenuation with distance and frequency (Green's function); and (d) the distance of the seismometer with the seismic source. In the VdN, turbulent noise is probably substantial in such a steep and rough channel, but a higher frequency band (25–60 Hz) was used to minimize the risk of signal contamination by turbulence (Text S4 in Supporting Information S1). To improve the inversion of bedload transport, seismometers were also located quite close to the stream (~5–30 m). The active seismic experiments also showed that the attenuation of the seismic signal with frequency was not too strong (Figure 5, Text S3 in Supporting Information S1). Finally, if the detection of individual small particles may be difficult in such a noisy environment, the collective motion and seismic noise emitted by small particles may add up to something detectable. We thus hypothesize that the difference in particle size detection threshold between the SPG system and the seismic inversion may also partly explain the greater magnitude bedload transport estimate based upon the seismic data at S1. Directly sampled data for this station (Antoniazza et al., 2022) showed that 20%–36% of the sample mass was on average composed of particles that were smaller than the threshold of detection of the SPG system. This interpretation may be further supported by the earlier onset of bedload transport estimated by seismic inversion (Figure 6, 10:00–11:00), if the onset of transport is size selective and small particles start moving first (Powell et al., 2001; Vericat et al., 2008). Nevertheless, it should be noted that the Tsai et al. (2012) model uses an analytical parameterization, which may not completely fit the distribution of the mobilized coarse material. In Alpine streams, the GSD is often bi-modal, with a peak in the sand fraction and a peak in the gravel fraction (Church et al., 1991; Flödl & Hauer, 2019; Hey & Thorne, 1986). As a consequence, there may be erroneous assumptions in the FMI with regards to GSD. The theoretical description of the GSD used by Tsai et al. (2012) may underestimate the seismic noise contribution of the largest particles (Lagarde et al., 2021; Turowski et al., 2015), which may lead to a prediction of lower noise for a given grain-size and hence to an overestimation of the inverted transport rate. This specific aspect will need to be better constrained in future research.

It is also possible that at very high transport rates the plates in the SPG are over-passed by some particle sizes (Rickenmann et al., 2012, 2014b), or the signal is saturated by simultaneous particle impacts (Coviello et al., 2022), which may also under-estimate the transport rate. At the tail of the event (>18:00 in Figure 6), greater bedload transport was estimated by the SPG system as compared to the seismic inversion. Looking at Figure 6a, we can observe in the seismic power spectrum that there is less seismic energy recorded at the tail of the event (>18:00) than there is in between the two bedload transport waves (13:30–15:00) in the bedload-specific frequency bands

(e.g., 40–50 Hz), while the radar-based water level is of comparable magnitude. Perhaps a change in grain-size or ground seismic properties at the tail of the event could cause a change in the signal-to-noise ratio, leading to an underestimate of the seismic-inverted bedload transport as compared to the SPG monitoring. Yet, this hypothesis is difficult to check quantitatively with the available data.

Despite those multiple potential sources of uncertainty affecting both monitoring systems, the difference between the seismic inversion of bedload transport and the SPG measurement is comparatively lower than that reported by Lagarde et al. (2021), and similar to that reported by Bakker et al. (2020), where seismic inversions of bedload transport were also compared with an independent measurement of bedload transport. Lagarde et al. (2021) compared their record with a Reid-type slot-sampler, using a similar seismic inversion approach to that applied here. They found differences in transport rate patterns as well as magnitudes with an average difference factor of 100 between instantaneous measures using the two methods. Their results likely reflected the grain-size limit of the slot-sampler (0.11 m), which may have inhibited the collection of the coarsest particles in transport (Lagarde et al. (2021), while the latter ($>D_{90}$) are assumed to be responsible for the largest proportion of the seismic signal recorded (Tsai et al., 2012). Bakker et al. (2020) used an Elwha pressure-difference sampler as their benchmark data, and applied a similar seismic inversion approach to the one used in this study. They reported a difference between the two monitoring systems within a factor of five, although the benchmark data were discrete in time, and not continuous as they are in this study.

A greater uncertainty may arise from the application of the seismic inversion approach to steep tributaries (e.g., S6, S11, S20, S23, S24). Macro-roughness in the channel and associated turbulence may overlap to a greater extent with the bedload transport frequency band used for the inversion (Roth et al., 2016; Schmandt et al., 2013, 2017). In addition, the possible occurrence of debris flow or debris flood in the tributaries may also increase the uncertainty, because the FMI is not yet specifically designed to handle this type of process, which may require different model assumptions with regards to particle impacts at the bed (Coviello et al., 2019; Farin et al., 2019; Schimmel et al., 2022; Yan et al., 2023). Yet, the relative coherence in the inverted bedload transport time-series between spatially consecutive seismic sensors and within individual tributaries (Figures 7–9), and the evidence that inverted bedload transport estimates before (<9:30) and after (>20:00) the event occurrence are close to zero at the 24 seismic sensor locations (Figures 7 and 8), suggests that the scaling of the event in absolute magnitude is encouraging. Further research should nevertheless develop and validate seismic inversion model for the specific case of steep and rough tributaries with possible debris flow and debris flood to better constrain the exact model capabilities (Coviello et al., 2019; Farin et al., 2019; Schimmel et al., 2022; Yan et al., 2023).

The relative good fit between the seismic-inverted bedload estimate and the independent SPG monitoring (Figure 6) provides therefore some confidence in the seismic inversion approach followed in this contribution. Yet, multiple sources of uncertainty remain and inverted bedload transport estimates should be considered with the necessary care, in particular in the absence of concurrent direct bedload transport samples. The timing of the event appears more accurate, while the absolute magnitude is subject to considerably more uncertainty. Given the difficulty of sampling directly bedload transport, future research should focus on better constraining the FMI model performance in different hydraulic and bedload transport conditions, so that control data are eventually no more required. Performing seismic monitoring of bedload transport in watersheds already equipped with a calibrated concurrent bedload transport monitoring system is likely a promising option. Yet, the fact that we can readily obtain time-varying bedload transport estimates at multiple locations across a watershed illustrates the potential for seismic approach to unpack the dynamics of bedload transport events in Alpine watersheds, and to possibly improve bedload transport predictions in the future by estimating changing coarse material availability in time and space.

4.2. Bedload Transport Event Anatomy

The spatially distributed time-varying estimates of bedload transport (Figures 7–9) allow a number of observations with respect to the anatomy of a relatively high-magnitude bedload transport event (return period 1–2 years) in a steep Alpine watershed.

4.2.1. Coarse Material Production in Headwater Tributaries

The inverted bedload transport estimates suggested that not every tributary was active to the same extent during the 3 August 2020 bedload transport event. Some tributaries dominated supply material during the studied event

(e.g., S4, S6, S11, S20, S21, and S22), and others had very low transport rates in comparison (i.e., S9, S15, and S19). The most active tributaries were not spatially contiguous even over what is a relatively small spatial area (maximum distance between any two tributary sensors is 2.5 km). Local tributary characteristics in terms of sediment availability may explain these differences, as well as local rainfall patterns (Michelon et al., 2021).

4.2.2. Attenuation in Bedload Transport Estimates Through the Watershed

The data set suggests that the basin itself rapidly attenuates (i.e., deposition occurs) the signal of hillslope erosion (Ganti et al., 2014; Jerolmack & Paola, 2010), in this case primarily due to the presence of hydraulically less-efficient alluvial fans (e.g., downstream from S11) and braided reaches (e.g., downstream of S16 and S17). Even large tributary inputs that would reach the main AdN channel are rapidly deposited to some extent (e.g., S6 tributary inputs to the main channel at S5 were largely attenuated by S3). These observations emphasize that attenuation of bedload transport is substantial for the studied bedload transport event, and that only a comparatively smaller proportion of the material mobilized in the watershed during the event is estimated as being exported to the outlet (~2.5%). This is notably a consequence of the profile of formerly glaciated landscapes, where the "staircase" succession of steeper (e.g., rockwalls, rockslopes, riegels) and flatter (glacier troughs) reaches significantly impact hydraulic efficiency (Antoniazza & Lane, 2021; S. J. Cook & Swift, 2012; Dell'Agnese et al., 2015; Hooke, 1991; Lane et al., 2017). There are few field data against which the present results can be compared, but the latter are in line with numerical simulations of coarse material transport in Alpine rivers, where large inputs from steep headwater tributaries were also rapidly deposited when reaching the flatter hydraulically less-efficient main channel network (Ferguson et al., 2006; Rickenmann et al., 2014a; Scorpio et al., 2022).

The attenuation of the bedload transport signal from headwater tributaries toward the outlet is also visible in the inversely proportional relationship between contributing area and the estimated mass of coarse material transported over the duration of the event (Figure 9c). It suggests a declining bedload Sediment Delivery Ratio with distance downstream which was to date has only been estimated in natural settings for suspended load (Brown, 1949; Wu et al., 2018). As implied above, a primary driver of this decline is the change in hydraulic efficiency (e.g., channel gradient, channel width) with the transition from steep tributaries to the main river (compare the bars on Figure 9c). It may also reflect increasing possibilities of storage with greater contributing area, and the possible occurrence of more transport-efficient processes (e.g., debris flow or debris flood) in the tributaries (Rickenmann & Koschni, 2010). The rate of attenuation is the greatest throughout the braided Reach 3 (down to S10), while the bedload transport estimates present less variability (Figures 7–9) through the mixed semi-alluvial and alluvial Reach 4 (Figure 1b). This relative constancy in bedload transport estimates through what is a quite long river reach (~2.8 km) is encouraging with regards to the development of "Early Warning systems" for bedload transport events along reaches of such morphology (A. Badoux et al., 2012; Chmiel et al., 2021).

4.2.3. Propagation of the Bedload Transporting Event

From Figure 10, we identified that the bedload transport event first started in sub-catchment (4) and was later fed by sub-catchment (5) and (6), with relatively more material estimated in (6). The analysis further emphasized the importance of tributary inputs for the timing and downstream propagation of the bedload transporting event, with coarse material supply from some tributaries (e.g., S11, S6, S4) occurring sometimes earlier than the bedload waves moving through the main AdN channel (Figure 10a). Analysis of inter-sensor propagation velocities (Figure 10b) showed a substantial variability, but tended to be greater in steep tributaries (e.g., S11 → S10, S19 → S17, S20 → S16, S22 → S18) than within flatter reaches of the main channel (e.g., S2 → S1, S8 → S7, S10 → S8, S12 → S10). Nevertheless, evidence of almost simultaneous bedload transport onset over sensors located multiple hundreds of meters away (e.g., S14 → S12, S16 → S13, S17 → S14, S18 → S14) questions the extent to which the same bedload material travels through the watershed and is sensed by multiple sensors, or whether we are rather facing a water wave that travels faster and (re-)mobilizes local coarse material.

Typical values of bedload particle step-lengths and velocities measured within Alpine watersheds during individual flooding events may give insights in this question. Vázquez-Tarrío et al. (2019) reviewed particle tracking experiments and compiled results from 217 episodes of bedload particle transport measured in 30 gravel-bed rivers, during floods of varying magnitude (dimensionless stream power from 1.5^{-2} to 1.5^{0} (–)), and along reaches with contrasting gradient (i.e., 0.1%–15%) and morphologies (i.e., riffle-pool, step-pool, plane-bed, multithread). Mean particle travel distance during individual floods ranged from a few meters to a few hundred meters, mostly less than 200 m (83% of events). In this study, seismometers were spaced from 268 to 882 m. Mao et al. (2017)

derived virtual bedload particle velocities (i.e., because of the possibility of resting periods in-between detections) between 10^{-5} and 35 m min^{-1} along a 13%-slope reach (plane-bed and step-pool morphology) of a glacier-fed river. Along a 4%-slope pool-riffle and step-pool river reach, Olinde and Johnson (2015) measured average particle step-lengths of 12.4 m and average transport duration of 0.5 min, which translated into an average velocity of ∼24 m min^{-1}, but particle steps were interspersed by resting periods that could last up to 190 hr. In this study, propagation velocities derived from consecutive seismic sensors ranged from 7 up to ∼100 m min^{-1}, outside of the previously identified sensor pairs where bedload transport was almost simultaneous.

It is well-known that bedload transport is an intermittent process, characterized by periods particle of motion interspersed by periods of rest, both following an exponential distribution with thin-tails (i.e., the bulk bedload moving roughly homogeneously, Einstein, 1937; Ganti et al., 2010, 2014; Hassan et al., 2013), although heavy-tailed super-diffusive distribution (i.e., few frontrunners being transported over larger distances than the bulk) have also been reported, typically over short durations (i.e., the flood scale, Hassan et al., 2013; Liébault et al., 2012; Phillips et al., 2013). The relatively long distance between the seismic sensors deployed in the frame of this study (268–882 m), as well as the relatively high propagation velocities derived from the cross-correlation analysis (7 up to ∼100 m min^{-1}), makes it quite unlikely that the same bulk bedload transport is actually able to travel at such pace throughout the watershed.

The slower velocities derived from the cross-correlation analysis (Figure 10b) fall within the same range as the higher velocities found in particle tracking experiments (Mao et al., 2017; Olinde & Johnson, 2015), which means that some frontrunner particles may have been transported over longer distances (Hassan et al., 2013) and were consecutively measured by multiple seismic sensors. Yet, it is more likely that the bulk bedload transport travels more slowly, and therefore that derived velocities correspond to the propagation of a water wave, which (re-)mobilizes locally coarse material that is then transported over shorter distances. This would suggest that fast water waves "leave behind" coarse material mobilized locally, which cannot handle such transport pace over long distances, possibly due to inter-particle collisions that slows it down (Hassan et al., 2013; Mao et al., 2017; Vázquez-Tarrío et al., 2019). Using seismic networks, K. L. Cook et al. (2018) estimated the water wave of a GLOF to travel at velocities between 300 and 540 m min^{-1}, and Chmiel et al. (2022) reported velocities of a flash-flood in France between 300 and 360 m min^{-1}. Although those events are relatively extreme, the faster propagation velocities we derived from cross-correlation analysis (e.g., S12 → S14, S13 → S16, S14 → S17, S14 → S18) are not out-of-bounds.

Previous hydrological research in the VdN Alpine watershed has shown, through combined piezometer network, thermal imaging from an uncrewed airborne vehicle, isotope analysis and hydrological modeling (Michelon et al., 2022; Thornton et al., 2022), that substantial groundwater release takes place in the VdN throughout Reach 3 (Figure 1b), where almost simultaneous bedload transport waves were measured in some instances between sensors spaced hundreds of meters away (e.g., S12 → S14, S14 → S17). Local hydrological conditions (e.g., notably associated with vertical hyporheic fluxes) may locally reduce the critical shear stress required for entrainment, and may increase sediment mobilization and transport capacity independently from the downstream propagation of the water wave, translating into simultaneous bedload transport mobilized at different locations of the watershed. The effect of groundwater release on coarse material mobilization deserves more attention in future research. Valuable knowledge of the respective propagation of water waves and bedload waves through Alpine watersheds may be gained from the deployment of distributed acoustic sensors, km-long fiber optic cables able to deliver seismic data almost continuously in space and time (Lior et al., 2021; Zhan, 2019).

4.3. Longer-Term Perspectives on Watershed-Scale Sedimentary Fluxes

The seismic sensor network deployed in the frame of this study revealed the anatomy of a relative high-magnitude bedload transport event (return period ∼1–2 years) in terms of coarse material production in headwater tributaries, bedload transport attenuation with travel down the watershed and event timing and propagation velocity. We now place these observations in a longer perspective of coarse material flux throughout Alpine watersheds with the help of the morphological change analysis.

During the studied event, with the fifth greatest bedload transport peak of the period 2016–2020, the proportion of coarse material estimated to be exported at the outlet was negligible (∼2.5%) compared to that inverted across the watershed, and notably in headwater tributaries, which suggests that substantial deposition took place

within the main channel network. Supply exceeded capacity and the event was deposition-dominated (Turowski et al., 2013). If such events were the rule, it would mean the main channel network would be aggrading on the longer term. This assertion can be related to the morphological change analysis (Figure 11). First, ∼88% of the material volume mobilized in the headwater tributaries are estimated to be exported at the outlet over the period 2016–2020, which is substantially more than the proportion derived during the 3 August event (∼2.5%). Thus, the general aggradation of the channel network estimated for the 3 August event cannot be the rule in longer bedload transport dynamics. Instead, material mobilized in headwater tributaries and deposited within the main channel network during high-magnitude events such as the one that occurred on 3 August 2020 appears to be progressively evacuated by subsequent competent flows, such as also observed in Scorpio et al. (2022). As reported as a characteristic of hillslope to river sediment transport coupling (Newson, 1980), lower competent flows than that reported here for the 3 August 2020 event may be more geomorphically effective because of the sediment delivered, but not evacuated during the event.

Second, results of the morphological change analysis suggest that a greater proportion of material exported from headwater tributaries is stored within alluvial fans (∼6%) over the period 2016–2020, than within the braided reach (∼1%) and the semi-alluvial reach (∼1%). During the 3 August 2020 event, substantial deposition was also observed within the braided river reach (Figures 8 and 9a). This suggests that in the longer term, material deposited within alluvial braided channel during high-magnitude events may be more easily reworked and exported during subsequent competent flows than the material deposited over the surface of alluvial fans.

Third, the fact that ∼96% of the watershed erosion takes place in the headwater tributary zone, and that little erosion proportionally occurs in the other morphological units (e.g., alluvial fans, braided channels, semi-alluvial channels) tends to confirm the view of Piton and Recking (2017) on the importance of "traveling bedload." Coarse material mobilized in distal headwater tributary sources seems to be transported in the main channel network without inducing in proportion major channel bed (re)working, in particular along alluvial fans and semi-alluvial reaches. The latter play a role of storage or conveyor, rather than acting as a sedimentary source. This trend was clear in the semi-alluvial reach during the 3 August event, where the estimated bedload transport magnitude was held relatively constant through a substantial length of channel (∼2.8 km; Figures 8 and 9a). This behavior can be related to the concept of "washload" developed for suspended load, consisting of particles found in the water column with sizes finer than the ones composing the bed (Piton & Recking, 2017; Turowski et al., 2010; Vanoni, 2006), mobilized in distal sources and conveyed through a main channel network that experiences in comparison little erosion or deposition (Comiti et al., 2019; Coviello et al., 2022). Note nevertheless that braided and semi-alluvial reaches may be more subject to compensating scour-fill effect (Lindsay & Ashmore, 2002) on the longer term, which may partly bias this observation.

High-magnitude events in the tributaries such as the ones that were estimated on 3 August 2020 may thus likely play an important role with regards to longer term coarse material fluxes. They indeed provide material into the main channel network from areas of the watershed where large sedimentary sources may be available (e.g., steep slopes at the top of rockwalls, tributary gullies, the glacier area), but which may not always be well connected during low to intermediate flows (Buter et al., 2022; Cavalli et al., 2013; Comiti et al., 2019; Lane et al., 2017). By supplying material into the main channel network, high-magnitude events in the tributaries may therefore supply new material, which appears to be remobilized during subsequent low, intermediate and high magnitude events in the main channel network (Cavalli et al., 2013; Lane et al., 2017; Turowski et al., 2013).

5. Conclusion

The way Alpine watersheds mobilize, convey and store coarse material is poorly constrained, which limits the accuracy of current bedload transport predictions. Environmental seismology applied to Alpine rivers, and combined with appropriate seismic physical models, provides estimates of time-varying bedload transport, with an average factor 4 of difference in this study when compared to an independent calibrated time-series of bedload transport. The 24 seismic sensors deployed during this study, and the spatially distributed time-varying estimates of bedload transport derived from them, have suggested a relative inefficiency of the VdN Alpine watershed in evacuating coarse material, even during what is a relatively infrequent high-magnitude bedload transport event (return period ∼1–2 years). Large inputs of sediment estimated through seismic inversion in some of the tributaries were indeed rapidly attenuated (i.e., deposition occurred) as the flow was crossing less hydraulically efficient reaches. Only a comparatively negligible proportion of the total amount of material mobilized in the

headwater tributaries was estimated to be exported at the outlet. Not every tributary transported bedload during the studied event, even at this small spatial scale, which underlines the importance of local hydrological and sediment availability conditions. The rapid propagation velocities derived from the cross-correlation analysis of the time-varying estimates of bedload suggested that a fast water wave was (re-)mobilizing local coarse material. Multiple periods of competent flows are thought to be necessary to evacuate the coarse material mobilized throughout the watershed during the studied event. High-magnitude bedload transport events in the tributaries nevertheless appeared to be important for supplying new material in the main channel network from poorly connected sourcing areas of the watershed, which are on the longer term progressively evacuated from it by subsequent competent flows.

The low cost, ease-of-deployment and ease-of-maintenance of seismometers means that environmental seismology may provide relatively reliable estimates of time-varying bedload transport at a very competitive price. Distributed seismic networks have the potential for tracking the motion of coarse material through Alpine watersheds and may help to constrain better and to improve prediction of bedload transport fluxes in the future, notably through the estimation of changing coarse material availability in space and time. Yet, the FMI model is still subject to various sources of uncertainty. These include the correct partitioning between turbulence and bedload transport frequency bands, the precision of the parameters the inversion model requires, the possible contamination of the bedload seismic signal by noise external to the river (e.g., rainfall), the spatial averaging of the bedload transport seismic signal over lengths of channel, and the possible discrepancy between the FMI assumptions and the processes taking place in steep and rough tributaries where debris flows could occur. As a result, estimates of bedload transport inverted from river seismic sensing, in particular where no concurrent control data are available, should be used with care. The timing of bedload transporting event appears to be less uncertain, while the absolute magnitude of inverted bedload transport estimates is subject to considerably more uncertainty. Future research should further test and validate the performance of the FMI under a range of different flow and bedload transport conditions.

Conflict of Interest

The authors declare no conflicts of interest relevant to this study.

Data Availability Statement

The seismic and SPG bedload transport data presented in the study (Figures made with Matlab v. R2019a and Adobe Illustrator 2023) will be made available online on the EnviDat repository https://www.envidat.ch/dataset/sediment-transport-observations-in-swiss-mountain-streams (Antoniazza et al., 2023) upon publication of the manuscript.

Acknowledgments
The authors thank the University of Lausanne and the Swiss National Science Foundation SNSF (Grant P1LAP2_194974 awarded to GA) for supporting this work. The University of Lausanne, the Swiss Federal Research Institute WSL, and the Physics of Environmental Systems group of the ETH Zürich are further thanked for financing the building of the SPG monitoring station at the Vallon de Nant. The Faculty of Geosciences and Environment of the University of Lausanne funded the acquisition of field equipment. The Geomorphology Section 4.6 at the GFZ Potsdam is thanked for hosting GA during his Doc.Mobility project, and for the support and expertise provided with environmental seismology data processing. The Geophysical Instrument Pool Potsdam (GIPP) of the GFZ provided seismic instruments (Grant GIPP202006-RAAC II). The authors are grateful to Magalí Matteodo, Mehdi Mattou, Floreana Miesen, Aurélien Ballu, Nora Krebs, Sabrina Hennig, François Bonnet, Valentin Quartenoud and family, Sylvain Bernard and family, and the team at "Auberge de Pont de Nant," for their support in the field. The authors are thankful to Mikaël Attal, Odin Marc, Francesco Comiti, and two anonymous reviewers for constructive and thoughtful reviews. Open access funding provided by Universite de Lausanne.

References

Altmann, M., Haas, F., Heckmann, T., Liébault, F., & Becht, M. (2021). Modelling of sediment supply from torrent catchments in the Western Alps using the sediment contributing area (SCA) approach. *Earth Surface Processes and Landforms*, *46*(5), 889–906. https://doi.org/10.1002/esp.5046

Ancey, C. (2020a). Bedload transport: A walk between randomness and determinism. Part 1. The state of the art. *Journal of Hydraulic Research*, *58*, 1–17. https://doi.org/10.1080/00221686.2019.1702594

Ancey, C. (2020b). Bedload transport: A walk between randomness and determinism. Part 2. Challenges and prospects. *Journal of Hydraulic Research*, *58*(1), 18–33. https://doi.org/10.1080/00221686.2019.1702595

Antoniazza, G., Bakker, M., & Lane, S. N. (2019). Revisiting the morphological method in two-dimensions to quantify bed-material transport in braided rivers. *Earth Surface Processes and Landforms*, *44*(11), 2251–2267. https://doi.org/10.1002/esp.4633

Antoniazza, G., Dietze, M., Mancini, D., Turowski, J., Rickenmann, D., Nicollier, T., et al. (2023). Anatomy of an Alpine bedload transport event: A watershed-scale seismic-network perspective [Dataset]. Envidat Repository. https://doi.org/10.1029/2022jf007000

Antoniazza, G., & Lane, S. N. (2021). Sediment yield over glacial cycles: A conceptual model. *Progress in Physical Geography: Earth and Environment*, *45*(6), 842–865. https://doi.org/10.1177/0309133321997292

Antoniazza, G., Nicollier, T., Boss, S., Mettra, F., Badoux, A., Schaefli, B., et al. (2022). Hydrological drivers of bedload transport in an Alpine watershed. *Water Resources Research*, *58*(3), e2021WR030663. https://doi.org/10.1029/2021WR030663

Antoniazza, G., Nicollier, T., Wyss, C. R., Boss, S., & Rickenmann, D. (2020). Bedload transport monitoring in alpine rivers: Variability in Swiss plate geophone response. *Sensors*, *20*(15), 4089. https://doi.org/10.3390/s20154089

Badoux, A., Andres, N., Techel, F., & Hegg, C. (2016). Natural hazard fatalities in Switzerland from 1946 to 2015. *Natural Hazards and Earth System Sciences*, *16*(12), 2747–2768. https://doi.org/10.5194/nhess-16-2747-2016

Badoux, A., Andres, N., & Turowski, J. (2014). Damage costs due to bedload transport processes in Switzerland. *Natural Hazards and Earth System Sciences*, *14*(2), 279–294. https://doi.org/10.5194/nhess-14-279-2014

Badoux, A., Turowski, J. M., Mao, L., Mathys, N., & Rickenmann, D. (2012). Rainfall intensity–duration thresholds for bedload transport initiation in small Alpine watersheds. *Natural Hazards and Earth System Sciences*, *12*(10), 3091–3108. https://doi.org/10.5194/nhess-12-3091-2012

Badoux, H. (1971). Feuille 1305 dent de Morcles.

Bakker, M., Antoniazza, G., Odermatt, E., & Lane, S. N. (2019). Morphological response of an Alpine braided reach to sediment-laden flow events. *Journal of Geophysical Research: Earth Surface*, *124*(5), 1310–1328. https://doi.org/10.1029/2018JF004811

Bakker, M., Gimbert, F., Geay, T., Misset, C., Zanker, S., & Recking, A. (2020). Field application and validation of a seismic bedload transport model. *Journal of Geophysical Research: Earth Surface*, *125*(5), e2019JF005416. https://doi.org/10.1029/2019JF005416

Bakker, M., Legout, C., Gimbert, F., Nord, G., Boudevillain, B., & Freche, G. (2022). Seismic modelling and observations of rainfall. *Journal of Hydrology*, *610*, 127812. https://doi.org/10.1016/j.jhydrol.2022.127812

Brown, C. B. (1949). Sediment transportation. In R. House (Ed.), *Engineering hydraulics* (pp. 769–857).

Burtin, A., Cattin, R., Bollinger, L., Vergne, J., Steer, P., Robert, A., et al. (2011). Towards the hydrologic and bed load monitoring from high-frequency seismic noise in a braided river: The "torrent de St Pierre", French Alps. *Journal of hydrology*, *408*(1–2), 43–53. https://doi.org/10.1016/j.jhydrol.2011.07.014

Burtin, A., Vergne, J., Rivera, L., & Dubernet, P. (2010). Location of river-induced seismic signal from noise correlation functions. *Geophysical Journal International*, *182*(3), 1161–1173. https://doi.org/10.1111/j.1365-246X.2010.04701.x

Buter, A., Heckmann, T., Filisetti, L., Savi, S., Mao, L., Gems, B., & Comiti, F. (2022). Effects of catchment characteristics and hydro-meteorological scenarios on sediment connectivity in glacierised catchments. *Geomorphology*, *402*, 108128. https://doi.org/10.1016/j.geomorph.2022.108128

Cavalli, M., Goldin, B., Comiti, F., Brardinoni, F., & Marchi, L. (2017). Assessment of erosion and deposition in steep mountain basins by differencing sequential digital terrain models. *Geomorphology*, *291*, 4–16. https://doi.org/10.1016/j.geomorph.2016.04.009

Cavalli, M., Trevisani, S., Comiti, F., & Marchi, L. (2013). Geomorphometric assessment of spatial sediment connectivity in small Alpine catchments. *Geomorphology, Sediment sources, source-to-sink fluxes and sedimentary budgets*, *188*, 31–41. https://doi.org/10.1016/j.geomorph.2012.05.007

Ceperley, N., Zuecco, G., Beria, H., Carturan, L., Michelon, A., Penna, D., et al. (2020). Seasonal snow cover decreases young water fractions in high Alpine catchments. *Hydrological Processes*, *34*(25), 4794–4813. https://doi.org/10.1002/hyp.13937

Chmiel, M., Godano, M., Piantini, M., Brigode, P., Gimbert, F., Bakker, M., et al. (2022). Brief communication: Seismological analysis of flood dynamics and hydrologically triggered earthquake swarms associated with Storm Alex. *Natural Hazards and Earth System Sciences*, *22*(5), 1541–1558. https://doi.org/10.5194/nhess-22-1541-2022

Chmiel, M., Walter, F., Wenner, M., Zhang, Z., McArdell, B. W., & Hibert, C. (2021). Machine learning improves debris flow warning. *Geophysical Research Letters*, *48*(3), e2020GL090874. https://doi.org/10.1029/2020GL090874

Church, M., Wolcott, J. F., & Fletcher, W. K. (1991). A test of equal mobility in fluvial sediment transport: Behavior of the sand fraction. *Water Resources Research*, *27*(11), 2941–2951. https://doi.org/10.1029/91WR01622

Comiti, F., Mao, L., Penna, D., Dell'Agnese, A., Engel, M., Rathburn, S., & Cavalli, M. (2019). Glacier melt runoff controls bedload transport in Alpine catchments. *Earth and Planetary Science Letters*, *520*, 77–86. https://doi.org/10.1016/j.epsl.2019.05.031

Cook, K. L., Andermann, C., Gimbert, F., Adhikari, B. R., & Hovius, N. (2018). Glacial lake outburst floods as drivers of fluvial erosion in the Himalaya. *Science*, *362*(6410), 53–57. https://doi.org/10.1126/science.aat4981

Cook, K. L., & Dietze, M. (2022). Seismic advances in process geomorphology. *Annual Review of Earth and Planetary Sciences*, *50*(1), 183–204. https://doi.org/10.1146/annurev-earth-032320-085133

Cook, S. J., & Swift, D. A. (2012). Subglacial basins: Their origin and importance in glacial systems and landscapes. *Earth-Science Reviews*, *115*(4), 332–372. https://doi.org/10.1016/j.earscirev.2012.09.009

Coviello, V., Arattano, M., Comiti, F., Macconi, P., & Marchi, L. (2019). Seismic characterization of debris flows: Insights into energy radiation and implications for warning. *Journal of Geophysical Research: Earth Surface*, *124*(6), 1440–1463. https://doi.org/10.1029/2018JF004683

Coviello, V., Vignoli, G., Simoni, S., Bertoldi, W., Engel, M., Buter, A., et al. (2022). Bedload fluxes in a glacier-fed river at multiple temporal scales. *Water Resources Research*, *58*(10), e2021WR031873. https://doi.org/10.1029/2021WR031873

Cucchiaro, S., Maset, E., Cavalli, M., Crema, S., Marchi, L., Beinat, A., & Cazorzi, F. (2020). How does co-registration affect geomorphic change estimates in multi-temporal surveys? *GIScience and Remote Sensing*, *57*(5), 611–632. https://doi.org/10.1080/15481603.2020.1763048

Dai, W., Xiong, L., Antoniazza, G., Tang, G., & Lane, S. N. (2021). Quantifying the spatial distribution of sediment transport in an experimental gully system using the morphological method. *Earth Surface Processes and Landforms*, *46*, 1188–1208. https://doi.org/10.1002/esp.5094

Dell'Agnese, A., Brardinoni, F., Toro, M., Mao, L., Engel, M., & Comiti, F. (2015). Bedload transport in a formerly glaciated mountain catchment constrained by particle tracking. *Earth Surface Dynamics*, *3*(4), 527–542. https://doi.org/10.5194/esurf-3-527-2015

Dietze, M. (2018). The R package "eseis"–a software toolbox for environmental seismology. *Earth Surface Dynamics*, *6*(3), 669–686. https://doi.org/10.5194/esurf-6-669-2018

Dietze, M., Bell, R., Ozturk, U., Cook, K. L., Andermann, C., Beer, A. R., et al. (2022a). More than heavy rain turning into fast-flowing water – A landscape perspective on the 2021 Eifel floods. *Natural Hazards and Earth System Sciences*, *22*(6), 1845–1856. https://doi.org/10.5194/nhess-22-1845-2022

Dietze, M., Hoffmann, T., Bell, R., Schrott, L., & Hovius, N. (2022b). A seismic approach to flood detection and characterization in upland catchments. *Geophysical Research Letters*, *49*(20), e2022GL100170. https://doi.org/10.1029/2022GL100170

Dietze, M., Lagarde, S., Halfi, E., Laronne, J., & Turowski, J. M. (2019). Joint sensing of bedload flux and water depth by seismic data inversion. https://doi.org/10.31223/osf.io/n5gcm

Downing, J. (2010). Acoustic gravel-momentum sensor. *US Geological Survey Scientific Investigations Report*, *5091*, 143–158.

Dutoit, A. (1983). *La végétation de l'étage subalpin du Vallon de Nant*. Université de Lausanne.

Egholm, D. L., Pedersen, V. K., Knudsen, M. F., & Larsen, N. K. (2012). Coupling the flow of ice, water, and sediment in a glacial landscape evolution model. *Geomorphology*, *141–142*, 47–66. https://doi.org/10.1016/j.geomorph.2011.12.019

Einstein, H. A. (1937). Bedload transport as a probability problem. *Sedimentation*, *1027*, C1–C105.

Farin, M., Tsai, V. C., Lamb, M. P., & Allstadt, K. E. (2019). A physical model of the high-frequency seismic signal generated by debris flows. *Earth Surface Processes and Landforms*, *44*(13), 2529–2543. https://doi.org/10.1002/esp.4677

Ferguson, R. I., Cudden, J. R., Hoey, T. B., & Rice, S. P. (2006). River system discontinuities due to lateral inputs: Generic styles and controls. *Earth Surface Processes and Landforms*, *31*(9), 1149–1166. https://doi.org/10.1002/esp.1309

Flödl, P., & Hauer, C. (2019). Studies on morphological regime conditions of bi-modal grain size rivers: Challenges and new insights for freshwater pearl mussel habitats. *Limnologica*, *79*, 125729. https://doi.org/10.1016/j.limno.2019.125729

Ganti, V., Lamb, M. P., & McElroy, B. (2014). Quantitative bounds on morphodynamics and implications for reading the sedimentary record. *Nature Communications*, *5*(1), 3298. https://doi.org/10.1038/ncomms4298

Ganti, V., Meerschaert, M. M., Foufoula-Georgiou, E., Viparelli, E., & Parker, G. (2010). Normal and anomalous diffusion of gravel tracer particles in rivers. *Journal of Geophysical Research*, *115*(F2), F00A12. https://doi.org/10.1029/2008JF001222

Gimbert, F., Fuller, B. M., Lamb, M. P., Tsai, V. C., & Johnson, J. P. L. (2019). Particle transport mechanics and induced seismic noise in steep flume experiments with accelerometer-embedded tracers. *Earth Surface Processes and Landforms*, *44*(1), 219–241. https://doi.org/10.1002/esp.4495

Gimbert, F., Tsai, V. C., & Lamb, M. P. (2014). A physical model for seismic noise generation by turbulent flow in rivers. *Journal of Geophysical Research: Earth Surface*, *119*(10), 2209–2238. https://doi.org/10.1002/2014JF003201

Gomez, B., & Soar, P. J. (2022). Bedload transport: Beyond intractability. *Royal Society Open Science*, *9*(3), 211932. https://doi.org/10.1098/rsos.211932

Hassan, M. A., Voepel, H., Schumer, R., Parker, G., & Fraccarollo, L. (2013). Displacement characteristics of coarse fluvial bed sediment. *Journal of Geophysical Research: Earth Surface*, *118*(1), 155–165. https://doi.org/10.1029/2012jf002374

Hey, R. D., & Thorne, C. R. (1986). Stable channels with mobile gravel beds. *Journal of Hydraulic Engineering*, *112*(8), 671–689. https://doi.org/10.1061/(ASCE)0733-9429(1986)112:8(671)

Hooke, R. L. (1991). Positive feedbacks associated with erosion of glacial cirques and overdeepenings. *GSA Bulletin*, *103*(8), 1104–1108. https://doi.org/10.1130/0016-7606(1991)103<1104:PFAWEO>2.3.CO;2

Jerolmack, D. J., & Paola, C. (2010). Shredding of environmental signals by sediment transport. *Geophysical Research Letters*, *37*(19), L19401. https://doi.org/10.1029/2010GL044638

Kreisler, A., Moser, M., Aigner, J., Rindler, R., Tritthart, M., & Habersack, H. (2017). Analysis and classification of bedload transport events with variable process characteristics. *Geomorphology*, *291*, 57–68. https://doi.org/10.1016/j.geomorph.2016.06.033

Lagarde, S., Dietze, M., Gimbert, F., Laronne, J. B., Turowski, J. M., & Halfi, E. (2021). Grain-size distribution and propagation effects on seismic signals generated by bedload transport. *Water Resources Research*, *57*(4), e2020WR028700. https://doi.org/10.1029/2020WR028700

Lane, S. N., Bakker, M., Gabbud, C., Micheletti, N., & Saugy, J.-N. (2017). Sediment export, transient landscape response and catchment-scale connectivity following rapid climate warming and Alpine glacier recession. *Geomorphology*, *277*, 210–227. https://doi.org/10.1016/j.geomorph.2016.02.015

Lane, S. N., Borgeaud, L., & Vittoz, P. (2016). Emergent geomorphic–vegetation interactions on a subalpine alluvial fan. *Earth Surface Processes and Landforms*, *41*(1), 72–86. https://doi.org/10.1002/esp.3833

Liébault, F., Bellot, H., Chapuis, M., Klotz, S., & Deschâtres, M. (2012). Bedload tracing in a high-sediment-load mountain stream. *Earth Surface Processes and Landforms*, *37*(4), 385–399. https://doi.org/10.1002/esp.2245

Lindsay, J., & Ashmore, P. (2002). The effects of survey frequency on estimates of scour and fill in braided river model. *Earth Surface Processes and Landforms*, *27*(1), 27–43. https://doi.org/10.1002/esp.282

Lior, I., Sladen, A., Rivet, D., Ampuero, J.-P., Hello, Y., Becerril, C., et al. (2021). On the detection capabilities of underwater distributed acoustic sensing. *Journal of Geophysical Research: Solid Earth*, *126*(3), e2020JB020925. https://doi.org/10.1029/2020JB020925

Mächler, E., Salyani, A., Walser, J.-C., Larsen, A., Schaefli, B., Altermatt, F., & Ceperley, N. (2021). Environmental DNA simultaneously informs hydrological and biodiversity characterization of an Alpine catchment. *Hydrology and Earth System Sciences*, *25*(2), 735–753. https://doi.org/10.5194/hess-25-735-2021

Mancini, D., & Lane, S. N. (2020). Changes in sediment connectivity following glacial debuttressing in an Alpine valley system. *Geomorphology*, *352*, 106987. https://doi.org/10.1016/j.geomorph.2019.106987

Mao, L., Dell'Agnese, A., & Comiti, F. (2017). Sediment motion and velocity in a glacier-fed stream. *Geomorphology*, *291*, 69–79. https://doi.org/10.1016/j.geomorph.2016.09.008

Maurer, J. M., Schaefer, J. M., Russell, J. B., Rupper, S., Wangdi, N., Putnam, A. E., & Young, N. (2020). Seismic observations, numerical modeling, and geomorphic analysis of a glacier lake outburst flood in the Himalayas. *Science Advances*, *6*(38), eaba3645. https://doi.org/10.1126/sciadv.aba3645

McArdell, B. W., Hirschberg, J., Graf, C., Boss, S., & Badoux, A. (2023). Illgraben debris-flow characteristics 2019-2022 - EnviDat [WWW Document]. Retrieved from https://www.envidat.ch/dataset/illgraben-debris-flow-characteristics-2019-2022

Météosuisse. (2017). Daily mean, minimum and maximum temperature: TabsD, TminD, TmaxD. Documentation of MeteoSwiss Grid-Data Products.

Météosuisse. (2019). Daily precipitation (final analysis): Rhires D. Documentation of MeteoSwiss. Grid-Data Products.

Michelon, A., Benoit, L., Beria, H., Ceperley, N., & Schaefli, B. (2021). Benefits from high-density rain gauge observations for hydrological response analysis in a small Alpine catchment. *Hydrology and Earth System Sciences*, *25*(4), 2301–2325. https://doi.org/10.5194/hess-25-2301-2021

Michelon, A., Ceperley, N., Beria, H., Larsen, J., Vennemann, T., & Schaefli, B. (2022). Studying the dynamic of a high Alpine catchment based on multiple natural tracers. *Hydrology and Earth System Sciences Discussions*, *2022*, 1–43. https://doi.org/10.5194/hess-2022-48

Minute, F., Comiti, F., & Cavalli, M. (2019). Assessing geomorphic changes induced by a debris-flow: A case study in the dolomites. *Rendiconti Online Societa Geologica Italiana*, *48*, 23–28. https://doi.org/10.3301/rol.2019.33

Mizuyama, T., Laronne, J. B., Nonaka, M., Sawada, T., Satofuka, Y., Matsuoka, M., et al. (2010). Calibration of a passive acoustic bedload monitoring system in Japanese mountain rivers. *US Geological Survey Scientific Investigations Report*, *5091*, 296–318.

Mueller, E. R., & Pitlick, J. (2005). Morphologically based model of bed load transport capacity in a headwater stream. *Journal of Geophysical Research*, *110*(F2), F02016. https://doi.org/10.1029/2003JF000117

Nativ, R., Turowski, J. M., Goren, L., Laronne, J. B., & Shyu, J. B. H. (2022). Influence of rarely mobile boulders on channel width and slope: Theory and field application. *Journal of Geophysical Research: Earth Surface*, *127*(9), e2021JF006537. https://doi.org/10.1029/2021JF006537

Newson, M. (1980). The geomorphological effectiveness of floods—A contribution stimulated by two recent events in mid-wales. *Earth Surface Processes*, *5*, 1–16. https://doi.org/10.1002/esp.3760050102

Nicollier, T., Antoniazza, G., Ammann, L., Rickenmann, D., & Kirchner, J. W. (2022). Toward a general calibration of the Swiss plate geophone system for fractional bedload transport. *Earth Surface Dynamics*, *10*(5), 929–951. https://doi.org/10.5194/esurf-2022-7

Nicollier, T., Antoniazza, G., Rickenmann, D., Hartlieb, A., & Kirchner, J. W. (2022). Improving the calibration of the Swiss plate geophone bedload monitoring system by filtering out seismic signals from extraneous particle impacts. *Earth and Space Science*, *9*(5), e2021EA001962. https://doi.org/10.1029/2021EA001962

Nicollier, T., Rickenmann, D., & Hartlieb, A. (2021). Field and flume measurements with the impact plate: Effect of bedload grain-size distribution on signal response. *Earth Surface Processes and Landforms*, *46*(8), 1504–1520. https://doi.org/10.1002/esp.5117

Olinde, L., & Johnson, J. P. L. (2015). Using RFID and accelerometer-embedded tracers to measure probabilities of bed load transport, step lengths, and rest times in a mountain stream. *Water Resources Research*, *51*(9), 7572–7589. https://doi.org/10.1002/2014WR016120

Phillips, C. B., Martin, R. L., & Jerolmack, D. J. (2013). Impulse framework for unsteady flows reveals superdiffusive bed load transport. *Geophysical Research Letters*, *40*(7), 1328–1333. https://doi.org/10.1002/grl.50323

Piantini, M., Gimbert, F., Bakker, M., Recking, A., & Nanni, U. (2022). Using a dense seismic array to study fluvial processes in a braided river reach under flood conditions. *LHB*, *108*(1), 2053314. https://doi.org/10.1080/27678490.2022.2053314

Picco, L., Mao, L., Rigon, E., Moretto, J., Ravazzolo, D., Delai, F., & Lenzi, M. A. (2012). An update of the sediment fluxes investigation in the Rio Cordon (Italy) after 25 years of monitoring. *Journal of Agricultural Engineering*, *43*(3), e17. https://doi.org/10.4081/jae.2012.e17

Piton, G., & Recking, A. (2017). The concept of travelling bedload and its consequences for bedload computation in mountain streams. *Earth Surface Processes and Landforms*, *42*(10), 1505–1519. https://doi.org/10.1002/esp.4105

Pitscheider, F., Comiti, F., Theule, J., Gems, B., & Cavalli, M. (2022). DoD applications in small mountain basins: Insights from the Gadria basin (Italy). ROL 58/2022. https://doi.org/10.3301/ROL.2022.19

Powell, D. M., Reid, I., & Laronne, J. B. (2001). Evolution of bed load grain size distribution with increasing flow strength and the effect of flow duration on the caliber of bed load sediment yield in ephemeral gravel bed rivers. *Water Resources Research*, *37*(5), 1463–1474. https://doi.org/10.1029/2000WR900342

Rainato, R., Mao, L., García-Rama, A., Picco, L., Cesca, M., Vianello, A., et al. (2017). Three decades of monitoring in the Rio Cordon instrumented basin: Sediment budget and temporal trend of sediment yield. *Geomorphology*, *291*, 45–56. https://doi.org/10.1016/j.geomorph.2016.03.012

Rainato, R., Mao, L., & Picco, L. (2018). Near-bankfull floods in an Alpine stream: Effects on the sediment mobility and bedload magnitude. *International Journal of Sediment Research*, *33*(1), 27–34. https://doi.org/10.1016/j.ijsrc.2017.03.006

Recking, A. (2013). An analysis of nonlinearity effects on bed load transport prediction. *Journal of Geophysical Research: Earth Surface*, *118*(3), 1264–1281. https://doi.org/10.1002/jgrf.20090

Recking, A., Leduc, P., Liébault, F., & Church, M. (2012). A field investigation of the influence of sediment supply on step-pool morphology and stability. *Geomorphology*, *139–140*, 53–66. https://doi.org/10.1016/j.geomorph.2011.09.024

Rickenmann, D. (2001). Comparison of bed load transport in torrents and gravel bed streams. *Water Resources Research*, *37*(12), 3295–3305. https://doi.org/10.1029/2001WR000319

Rickenmann, D. (2017). Bedload transport measurements with geophones, hydrophones and underwater microphones (passive acoustic methods). In *Gravel bed rivers and disasters* (pp. 185–208). Wiley & Sons.

Rickenmann, D. (2018). Variability of bed load transport during six summers of continuous measurements in two Austrian mountain streams (Fischbach and Ruetz). *Water Resources Research*, *54*(1), 107–131. https://doi.org/10.1002/2017WR021376

Rickenmann, D. (2020). Effect of sediment supply on cyclic fluctuations of the disequilibrium ratio and threshold transport discharge, inferred from bedload transport measurements over 27 Years at the Swiss Erlenbach stream. *Water Resources Research*, *56*(11), e2020WR027741. https://doi.org/10.1029/2020WR027741

Rickenmann, D. (2023). Bedload transport fluctuations, flow conditions and disequilibrium ratio at the Swiss Erlenbach stream: Results from 27 years of high-resolution temporal measurements. *EGUsphere*, *2023*, 1–36. https://doi.org/10.5194/egusphere-2023-964

Rickenmann, D., Heimann, F. U. M., Turowski, J. M., Bieler, C., Böckli, M., & Badoux, A. (2014a). Simulation of bedload transport in the Hasliaare River with increased sediment input. In *River flow* (pp. 2273–2281).

Rickenmann, D., & Koschni, A. (2010). Sediment loads due to fluvial transport and debris flows during the 2005 flood events in Switzerland. *Hydrological Processes: International Journal*, *24*(8), 993–1007. https://doi.org/10.1002/hyp.7536

Rickenmann, D., Turowski, J. M., Fritschi, B., Klaiber, A., & Ludwig, A. (2012). Bedload transport measurements at the Erlenbach stream with geophones and automated basket samplers. *Earth Surface Processes and Landforms*, *37*(9), 1000–1011. https://doi.org/10.1002/esp.3225

Rickenmann, D., Turowski, J. M., Fritschi, B., Wyss, C., Laronne, J., Barzilai, R., et al. (2014b). Bedload transport measurements with impact plate geophones: Comparison of sensor calibration in different gravel-bed streams. *Earth Surface Processes and Landforms*, *39*(7), 928–942. https://doi.org/10.1002/esp.3499

Roth, D. L., Brodsky, E. E., Finnegan, N. J., Rickenmann, D., Turowski, J. M., & Badoux, A. (2016). Bed load sediment transport inferred from seismic signals near a river. *Journal of Geophysical Research: Earth Surface*, *121*(4), 725–747. https://doi.org/10.1002/2015JF003782

Schimmel, A., Coviello, V., & Comiti, F. (2022). Debris flow velocity and volume estimations based on seismic data. *Natural Hazards and Earth System Sciences*, *22*(6), 1955–1968. https://doi.org/10.5194/nhess-22-1955-2022

Schmandt, B., Aster, R. C., Scherler, D., Tsai, V. C., & Karlstrom, K. (2013). Multiple fluvial processes detected by riverside seismic and infrasound monitoring of a controlled flood in the Grand Canyon. *Geophysical Research Letters*, *40*(18), 4858–4863. https://doi.org/10.1002/grl.50953

Schmandt, B., Gaeuman, D., Stewart, R., Hansen, S. M., Tsai, V. C., & Smith, J. (2017). Seismic array constraints on reach-scale bedload transport. *Geology*, *45*(4), 299–302. https://doi.org/10.1130/g38639.1

Schneider, J. M., Rickenmann, D., Turowski, J. M., Bunte, K., & Kirchner, J. W. (2015). Applicability of bed load transport models for mixed-size sediments in steep streams considering macro-roughness. *Water Resources Research*, *51*(7), 5260–5283. https://doi.org/10.1002/2014WR016417

Schneider, J. M., Turowski, J. M., Rickenmann, D., Hegglin, R., Arrigo, S., Mao, L., & Kirchner, J. W. (2014). Scaling relationships between bed load volumes, transport distances, and stream power in steep mountain channels. *Journal of Geophysical Research: Earth Surface*, *119*(3), 533–549. https://doi.org/10.1002/2013JF002874

Scorpio, V., Cavalli, M., Steger, S., Crema, S., Marra, F., Zaramella, M., et al. (2022). Storm characteristics dictate sediment dynamics and geomorphic changes in mountain channels: A case study in the Italian Alps. *Geomorphology*, *403*, 108173. https://doi.org/10.1016/j.geomorph.2022.108173

Swisstopo. (2022). *SwissAlti3d - Le modèle de terrain à haute résolution de la Suisse*. Wabern.

Thornton, J. M., Brauchli, T., Mariethoz, G., & Brunner, P. (2021). Efficient multi-objective calibration and uncertainty analysis of distributed snow simulations in rugged Alpine terrain. *Journal of Hydrology*, *598*, 126241. https://doi.org/10.1016/j.jhydrol.2021.126241

Thornton, J. M., Mariethoz, G., & Brunner, P. (2018). A 3D geological model of a structurally complex Alpine region as a basis for interdisciplinary research. *Scientific Data*, *5*(1), 180238. https://doi.org/10.1038/sdata.2018.238

Thornton, J. M., Therrien, R., Mariéthoz, G., Linde, N., & Brunner, P. (2022). Simulating fully-integrated hydrological dynamics in complex lpine headwaters: Potential and challenges. *Water Resources Research*, *58*(4), e2020WR029390. https://doi.org/10.1029/2020WR029390

Tsai, V. C., Minchew, B., Lamb, M. P., & Ampuero, J.-P. (2012). A physical model for seismic noise generation from sediment transport in rivers. *Geophysical Research Letters*, *39*(2), L02404. https://doi.org/10.1029/2011GL050255

Turowski, J. M. (2012). Semi-alluvial channels and sediment-flux-driven bedrock erosion. In *Gravel-bed rivers* (pp. 399–418). John Wiley & Sons, Ltd. https://doi.org/10.1002/9781119952497.ch29

Turowski, J. M., Badoux, A., Leuzinger, J., & Hegglin, R. (2013). Large floods, alluvial overprint, and bedrock erosion. *Earth Surface Processes and Landforms*, *38*(9), 947–958. https://doi.org/10.1002/esp.3341

Turowski, J. M., Rickenmann, D., & Dadson, S. J. (2010). The partitioning of the total sediment load of a river into suspended load and bedload: A review of empirical data. *Sedimentology*, *57*(4), 1126–1146. https://doi.org/10.1111/j.1365-3091.2009.01140.x

Turowski, J. M., Wyss, C. R., & Beer, A. R. (2015). Grain size effects on energy delivery to the streambed and links to bedrock erosion. *Geophysical Research Letters*, *42*(6), 1775–1780. https://doi.org/10.1002/2015GL063159

Turowski, J. M., Yager, E. M., Badoux, A., Rickenmann, D., & Molnar, P. (2009). The impact of exceptional events on erosion, bedload transport and channel stability in a step-pool channel. *Earth Surface Processes and Landforms*, *34*(12), 1661–1673. https://doi.org/10.1002/esp.1855

Vanoni, V. A. (2006). *Sedimentation engineering*. American Society of Civil Engineers. https://doi.org/10.1061/9780784408230

Vázquez-Tarrío, D., Recking, A., Liébault, F., Tal, M., & Menéndez-Duarte, R. (2019). Particle transport in gravel-bed rivers: Revisiting passive tracer data. *Earth Surface Processes and Landforms*, *44*(1), 112–128. https://doi.org/10.1002/esp.4484

Vericat, D., Batalla, R. J., & Gibbins, C. N. (2008). Sediment entrainment and depletion from patches of fine material in a gravel-bed river. *Water Resources Research*, *44*(11), W11415. https://doi.org/10.1029/2008WR007028

Vittoz, P., & Gmür, P. (2009). *Introduction aux Journées de la biodiversité dans le Vallon de Nant (Bex, Alpes vaudoises)*. undefined.

Walter, F., Burtin, A., McArdell, B. W., Hovius, N., Weder, B., & Turowski, J. M. (2017). Testing seismic amplitude source location for fast debris-flow detection at Illgraben, Switzerland. *Natural Hazards and Earth System Sciences*, *17*(6), 939–955. https://doi.org/10.5194/nhess-17-939-2017

Welch, P. (1967). The use of fast Fourier transform for the estimation of power spectra: A method based on time averaging over short, modified periodograms. *IEEE Transactions on Audio and Electroacoustics*, *15*(2), 70–73. https://doi.org/10.1109/TAU.1967.1161901

Wohl, E. (2006). Human impacts to mountain streams. *Geomorphology*, *79*(3–4), 217–248. https://doi.org/10.1016/j.geomorph.2006.06.020

Wohl, E. (2013). *Mountain rivers revisited*. John Wiley & Sons.

Wolman, M. G. (1954). A method of sampling coarse river-bed material. *EOS, Transactions American Geophysical Union*, *35*(6), 951–956. https://doi.org/10.1029/tr035i006p00951

Wu, L., Liu, X., & Ma, X. (2018). Research progress on the watershed sediment delivery ratio. *International Journal of Environmental Studies*, *75*(4), 565–579. https://doi.org/10.1080/00207233.2017.1392771

Wyss, C. R., Rickenmann, D., Fritschi, B., Turowski, J. M., Weitbrecht, V., & Boes, R. M. (2016a). Laboratory flume experiments with the Swiss plate geophone bed load monitoring system: 1. Impulse counts and particle size identification. *Water Resources Research*, *52*(10), 7744–7759. https://doi.org/10.1002/2015WR018555

Wyss, C. R., Rickenmann, D., Fritschi, B., Turowski, J. M., Weitbrecht, V., & Boes, R. M. (2016b). Measuring bed load transport rates by grain-size fraction using the Swiss plate geophone signal at the Erlenbach. *Journal of Hydraulic Engineering*, *142*, 04016003. https://doi.org/10.1061/(ASCE)HY.1943-7900.0001090

Wyss, C. R., Rickenmann, D., Fritschi, B., Turowski, J. M., Weitbrecht, V., Travaglini, E., et al. (2016c). Laboratory flume experiments with the Swiss plate geophone bed load monitoring system: 2. Application to field sites with direct bed load samples. *Water Resources Research*, *52*(10), 7760–7778. https://doi.org/10.1002/2016WR019283

Yager, E. M., Dietrich, W. E., Kirchner, J. W., & McArdell, B. W. (2012). Prediction of sediment transport in step-pool channels. *Water Resources Research*, *48*(1), W01541. https://doi.org/10.1029/2011WR010829

Yager, E. M., Kenworthy, M., & Monsalve, A. (2015). Taking the river inside: Fundamental advances from laboratory experiments in measuring and understanding bedload transport processes. *Geomorphology*, *244*, 21–32. https://doi.org/10.1016/j.geomorph.2015.04.002

Yan, Y., Tang, H., Hu, K., Turowski, J. M., & Wei, F. (2023). Deriving debris-flow dynamics from real-time impact-force measurements. *Journal of Geophysical Research: Earth Surface*, *128*(3), e2022JF006715. https://doi.org/10.1029/2022JF006715

Zhan, Z. (2019). Distributed acoustic sensing turns fiber-optic cables into sensitive seismic antennas. *Seismological Research Letters*, *91*, 1–15. https://doi.org/10.1785/0220190112